HHS Public Access

Author manuscript

Dev Cell. Author manuscript; available in PMC 2024 February 27.

Published in final edited form as:

Dev Cell. 2023 February 27; 58(4): 306–319.e5. doi:10.1016/j.devcel.2023.01.008.

Runx1 Controls Auditory Sensory Neuron Diversity in Mice

Brikha R Shrestha[1,2,3,4,*], **Lorna Wu**[1], **Lisa V Goodrich**[1,4,5,*]

[1]Department of Neurobiology, Harvard Medical School, Boston, MA, 02115, United States

[2]Eaton-Peabody Laboratories, Massachusetts Eye and Ear, Boston, MA, 02114, United States

[3]Department of Otolaryngology, Harvard Medical School, Boston, MA, 02114, United States

[4]Senior authors

[5]Lead contact

Summary

Sound stimulus is encoded in mice by three molecularly and physiologically diverse subtypes of sensory neurons, called Ia, Ib, and Ic spiral ganglion neurons (SGNs). Here, we show that the transcription factor Runx1 controls SGN subtype composition in the murine cochlea. *Runx1* is enriched in Ib/Ic precursors by late embryogenesis. Upon loss of *Runx1* from embryonic SGNs (*Runx1*^{CKO}), more SGNs take on Ia rather than Ib or Ic identities. This conversion was more complete for genes linked to neuronal function than to connectivity. Accordingly, synapses in the Ib/Ic location acquired Ia properties. Suprathreshold SGN responses to sound were enhanced in *Runx1*^{CKO} mice, confirming expansion of neurons with Ia-like functional properties. *Runx1* deletion after birth also redirected Ib/Ic SGNs towards Ia identity, indicating that SGN identities are plastic postnatally. Altogether, these findings show that diverse neuronal identities essential for normal auditory stimulus coding arise hierarchically and remain malleable during postnatal development.

Graphical Abstract

*Correspondence: Brikha_Shrestha@meei.harvard.edu or Lisa_Goodrich@hms.harvard.edu.

Author Contributions

B.R.S. conceived and supervised the project, designed the experiments, performed scRNA-seq, analyzed the data, secured funding, and prepared the manuscript. L.W. performed all experiments except scRNA-seq, analyzed the data, and prepared the manuscript. L.V.G. conceived and supervised the project, secured funding, and prepared the manuscript.

Declaration of interests

The authors declare no competing interests.

Inclusion and Diversity

We support inclusive, diverse, and equitable conduct of research.

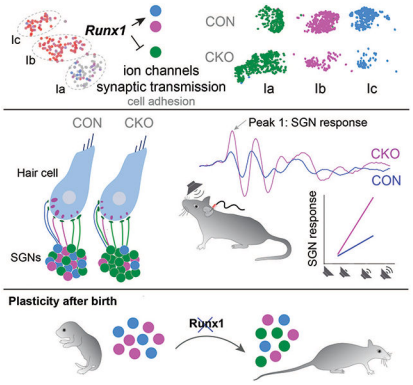

eTOC blurb

Shrestha et al identify the transcription factor Runx1 as a molecular switch that controls generation and postnatal maintenance of neuron subtype identities necessary for encoding sound in mice.

Keywords

plasticity; neuronal identity; auditory; cochlea; spiral ganglion neurons; Runx1

Introduction

Across sensory systems, the burden of encoding stimuli is split among sensory neuron subpopulations with functional differences in their response sensitivity and input-output relationships. Such diversity constitutes a key circuit motif upon which a broad range of stimulus features are functionally mapped. For example, in the auditory periphery, Type I spiral ganglion neurons (SGNs) with different response thresholds collectively encode the wide range of sound intensities an animal may encounter[1–3]. These neurons are classified based on transcriptomic profiles into three major subtypes (Ia, Ib, Ic)[4–6]. Based on anatomy, these subtypes correspond to physiologically-defined groups with high-, medium-, and low-spontaneous rates (SR) and low-to-high thresholds, respectively, for sound-driven response[7]. Degeneration of Ic SGNs or loss of their synapses after sound overexposure[8] and in old age[4,9] is thought to cause perceptual deficits, given the proposed significance of this SGN subtype for hearing against background noise[10–12] and of complex sounds[2]. It is therefore believed that the full range of SGN subtype diversity is essential for high-fidelity auditory perception. However, it remains unclear how a stereotyped distribution of SGNs with physiologically distinct properties is established.

During neural development, transcription factors (TFs) act sequentially to produce functionally and morphologically distinct types of neurons[13–15]. Early acting TFs direct neuronal progenitors towards progressively more restricted fates, ultimately activating sets of TFs that induce cohorts of genes needed for mature function. For instance, the TF Gata3 steers inner ear neuronal progenitors towards an auditory fate[16] and activates expression of effector TFs, such as Mafb, which controls the formation of synapses with inner hair cells (IHCs)[17]. Additionally, TFs likely act in a subtype-specific manner to generate Ia, Ib,

and Ic SGNs that exhibit physiological and anatomical differences. For example, *Pou4f1* is restricted to Ib and Ic SGNs[4]. Loss of *Pou4f1* in SGNs alters presynaptic features in the IHCs[18] but does not affect other aspects of subtype identity. Ia, Ib, and Ic precursors are distinguishable based on their molecular profiles by late embryogenesis in mice.[19,20] Subtype-specific patterns of gene expression continue to be refined during the first postnatal week[4], and individual neurons do not exhibit mature physiological properties and synaptic heterogeneity until the end of the first month.[21] Further, the postnatal consolidation of SGN subtype identity is both flexible and activity-dependent, as more SGNs acquire Ia identities when IHC-SGN signaling is disrupted.[4,6] Thus, unidentified TFs likely coordinate acquisition of subtype identity in the spiral ganglion, perhaps in response to activity or other signals in the environment.

An excellent candidate for SGN diversification is the TF Runx1, which is detected in Ib and Ic SGNs but not Ia SGNs[4]. Likewise, *Runx1* is restricted to subsets of developing dorsal root ganglion (DRG) neurons and promotes the non-peptidergic nociceptive identity within this population[22,23]. In this role, Runx1 acts both as transcriptional activator and repressor, regulating a battery of ion channel and receptor genes, i.e. genes that could impart functional differences among DRG neurons.[22] Notably, in this system, Runx1 functions at the nexus of cell-intrinsic and extrinsic (nerve growth factor-driven) signals to regulate gene transcription associated with non-peptidergic identity[24]. Furthermore, Runx1 regulates postmitotic cell fate decisions in other cell types, with important roles in definitive hematopoiesis and specification of T lymphocytes in the thymus.[25]

Here, we investigated the role of *Runx1* in diversification of Type I SGNs in the mouse cochlea. We found that, upon ablation of *Runx1* function, Ib and Ic identities are significantly depleted without overt neuronal loss, resulting in overabundance of Ia identity. This change in proportions of SGN subtypes is consequential for sound encoding at the auditory nerve, as mutant animals exhibit heightened neural responses to suprathreshold stimuli. In addition, fate-mapping revealed that *Runx1*-positive precursors are biased to become Ib/Ic SGNs by birth and that this expression must be maintained postnatally for Ib and Ic SGNs to hold on to their nascent identities. Together, these findings show that plasticity in neuronal identity contributes to neural circuit formation and identify *Runx1* as a key regulator of neural diversity in the auditory periphery subserving sound encoding.

Results

In considering how Type I SGN diversity is generated, *Runx1* stood out as a strong candidate given its enrichment in Ib/Ic SGNs[4,5] (Fig. 1A) and known roles in determining alternative cell fates in other systems. Since transcriptional identities of Type I SGNs begin to coalesce embryonically,[4,5,19] we reasoned that if *Runx1* is involved in regulating SGN identities, it may exhibit segregated expression before birth.

We surveyed *Runx1* expression in spiral ganglia of *bhlhe22*^{Cre}/+;*Ai14*/+ mice starting at E14.5, when SGN peripheral processes have almost reached IHCs (Fig. 1B).[26,27] *Runx1* was broadly expressed by SGNs as early as E14.5 and then became progressively restricted, with clear heterogeneity in *Runx1* levels by E18.5. Molecularly distinct SGNs that are

OFF for *Lypd1* and express high levels of *Calb2* (Fig. 1C,D), consistent with their complementary expression in mature Ia SGNs, were also detected by then.[4] At birth, SGNs that maintain *Runx1* tend to show strong *Lypd1* expression (Fig. 1E,F). Thus, perinatally, *Runx1* expression already overlaps with the Type Ic marker *Lypd1* and is biased toward cells with lower *Calb2* levels. This indicates that spatiotemporal changes in *Runx1* expression coincide with the emergence of molecularly distinct SGNs.

To determine the fates of precursors that express *Runx1* during SGN diversification, we used *Runx1*^{CreER} mice, which produce CreER under control of the endogenous *Runx1* locus[28] (Fig. 1G). *Runx1*^{CreER}/+;*Ai3*/+ mice were administered Tamoxifen at E15.5 to genetically tag Runx1^{+} SGNs with YFP (Fig. 1H). Evaluation of SGN identity by RNAscope for *Lypd1* and *Calb2* revealed that many neurons that were *Runx1*$^{+}$ at E15.5 had taken on Ib (*Calb2*^{MID} *Lypd1*^{OFF}) or Ic (*Calb2*^{LOW} *Lypd1*^{ON}) identities at P25 (Fig. 1I,J). These results hint that *Runx1* may influence the generation of molecularly diverse SGNs.

Effect of *Runx1* loss on SGN molecular identity

To test whether *Runx1* is necessary for SGN heterogeneity, we abolished *Runx1* function in SGNs by pairing *bhlhe22*^{Cre},[29] which drives expression of Cre recombinase in SGNs by E9.5[16], with homozygous floxed *Runx1* alleles (*Runx1*$^{F/F}$)[30] and a fluorescent tdTomato reporter (*Ai14*). This approach should delete exon 4 of *Runx1*, thereby ablating the Runt domain critical for its DNA- and cofactor-binding abilities[30], and simultaneously result in tdTomato expression in SGNs. Unlike *Runx1*$^{-/-}$ mice that die by E12.5[31], *Runx1*^{CKO} mice are viable and show no obvious behavioral deficits. SGN identities were assessed by single cell RNA-sequencing (scRNA-seq) of tdTomato^{+} neurons from young adult mice (P30-P33) enriched from single cell dissociates of the entire cochlea by fluorescence-activated cell sorting (FACS) (Fig. 2A). The resulting transcriptomic libraries showed a clear reduction in cDNA reads mapping to exon 4 of *Runx1* (Fig. S1A), indicating loss of functional Runx1 in most CKO neurons. Some exon 4 reads were still observed, suggesting that a small proportion did not undergo Cre-induced recombination. Both dimension reduction by Uniform Manifold Approximation and Projection (UMAP) and graph-based clustering of transcriptomic profiles revealed four molecularly distinct SGN subgroups in control animals (Fig. 2B). Three subgroups corresponded to Type Ia, Ib, Ic identities and the fourth had a Type II molecular profile. Subtype markers were expressed in expected patterns (Fig. 2C), indicating that this workflow faithfully captured cell types and gene expression states that represent the major source of molecular heterogeneity among these neurons described previously.[4]

scRNA-seq analysis of SGNs from *Runx1*^{CKO} animals revealed a striking difference in the distribution of subtype identities despite similarity in overall cDNA library quality compared to control (Fig. S1B,C). The mutant SGNs segregated into the same four classes, with one Type II and three Type I clusters that overlap with those from control animals in UMAP space (Fig. S1D,E). However, although all three Type I subgroups could be detected, the relative proportions of SGN subtypes was significantly altered: whereas Ia, Ib, Ic neurons were 26.4%, 40.2%, 33.4% of total Type I SGNs in controls, they made up 76.6%, 13.7%, 9.7% in *Runx1*^{CKO} animals, respectively (Fig. S1E, 2D–E). These changes constitute a

90% increase in Ia SGN proportion, and 66% and 71% decreases in those of Ib and Ic SGNs respectively. Thus, precursors that would normally take on Ib or Ic identities seem to develop instead as Ia SGNs. This change in distribution cannot be explained by technical variables, as cluster identities did not correlate with measures of single cell library quality and complexity such as number of mRNA and number of genes detected (Fig. S1F,G). Cells in the expanded Ia cluster expressed Ia-enriched genes (Fig. 2F) and downregulated Ib and Ic markers (Fig. S1H). This shift to a Ia-like profile included some genes that turned on or off and others that changed to levels typical of Ia identity (Fig. S1I). Moreover, mutant neurons maintained differential expression of Type I (*Epha4*) vs. Type II (*Cilp*) SGN markers (Fig. 2F), indicating that the key change was a switch to Ia identity. This interpretation held true even when gene expression trends were analyzed without assigning cluster identity: compared to controls, more *Runx1*^{CKO} neurons expressed Ia-enriched genes at higher levels while the opposite was true for Ib/Ic markers (Fig. 2G).

Independent assessment of the SGN phenotype further suggests that the change in neuronal proportions is due to a conversion of Ib/Ic SGNs into Ia SGNs. To explore whether changes in cell survival might account for altered SGN subtype proportions in *Runx1*^{CKO} animals, we measured neuronal density, an approach that has been used successfully to assay neuron loss in murine spiral ganglia.[4,32,33] We found no evidence of neuron loss: SGN density in *Runx1*^{CKO} animals was statistically indistinguishable from that in controls (Fig. 2H, S1J). Next, we assessed identity *in situ* by performing RNAscope for the subtype markers *Calb2* and *Lypd1* on cryosections of the cochlea. To interpret these results, K-means clustering was performed on cell-specific gene expression levels determined by quantitative analysis of fluorescent RNAscope puncta using Imaris. SGNs in control animals could be classified into three distinct subgroups (Fig. 2I,J). Consistent with previous reports based on transcriptional profiling[4–6], the subgroups marked by *Calb2*^{MID}, *Lypd1*^{OFF} (Ib) and *Calb2*^{LOW}, *Lypd1*^{ON} (Ic) comprised nearly 2/3rd of the total SGN population. A support vector machine (SVM)-based classifier built using control data (inset in Fig. 2J, see Methods) grouped *Runx1*^{CKO} SGNs (Fig. S1K) into the same three subgroups, albeit at clearly different proportions —*Calb2*^{HI}*Lypd1*^{OFF} Ia SGNs were overrepresented by 77% compared to controls, with marked reduction of *Calb2*^{LOW} *Lypd1*^{ON} Ic identities (Fig. 2K). Taken together, these results support the conclusion that overabundance of Ia SGNs in mice lacking functional *Runx1* in SGNs arises from aberrant apportioning of neuronal molecular identities during development.

Mixed identities and hierarchical plasticity of gene expression

Neuronal identities can be defined along multiple facets such as connectivity, metabolic signatures, synaptic properties, and intrinsic physiology[34]. Previous work has shown that, among DRG sensory neurons, Runx1 controls non-peptidergic nociceptive neuron identity by regulating both ion channel profiles and innervation patterns within the dorsal horn.[22] This raises the possibility that Runx1 likewise coordinates multiple aspects of SGN identities.

Closer examination of gene expression patterns revealed that Runx1 can have variable effects on SGN subtype identity. By comparison to control Ia, Ib, and Ic SGNs, some

Runx1^{CKO} Ia SGNs seemed to show complete conversion to the Ia identity: these SGNs expressed many Ia-enriched genes, such as *Calb2*, *Cacna1b*, *Rxrg*, *B3gat1* (Fig. 2F), and also did not express Ib/Ic-enriched genes, such as *Kcnip2*, *Nalcn*, *Ncald,* and *Slit2* (Fig. S1H). However, other SGNs in the Ia cluster failed to downregulate all Ib/Ic genes – *Ntng1*, *Lypd1*, and *Grm8* expression was retained in a subset of *Runx1*^{CKO} SGNs that otherwise matched Ia SGNs (Fig. 3A). A broader look at subtype-specific differentially expressed (DE) genes indicated similar trends for more genes, particularly ones that are Ic-enriched (purple arrows in Fig. S1I). Thus, not all genes changed in patterns expected for the change in subtype profiles, raising the possibility that some *Runx1*^{CKO} SGNs took on mixed identities.

To define whether SGNs are cleanly cast into one of three possible molecular identities in *Runx1*^{CKO} animals, as happens in wildtype animals by the 4th postnatal week, we performed supervised clustering of SGN scRNA-seq profiles. Cell identities were assigned based on ensemble learning using DE genes. To improve the fidelity of cell class prediction, random gene pairs—as opposed to individual genes—were used to derive a top-pair random forest classifier (TP-RF) (see Methods). We first used the classifier built using all DE genes (n=508) to predict SGN identities in test data from control animals. Considering results of unsupervised clustering as the ground truth, the classifier performed at 98% accuracy overall; only 5% of the 2% error was attributable to incorrectly assigning Ia identity to cells. When applied to *Runx1*^{CKO} SGNs, the classifier yielded predictions in which the proportions of Ia, Ib, Ic SGNs were 55%, 13%, and 10%, respectively (Fig. 3B). This represents nearly a doubling of the proportion of Ia SGNs, which normally comprise only ~25% of the population. In addition, 22% of the mutant SGNs were of mixed identity. Nearly all of these mixed cells belonged to the Ia group in a UMAP two-dimensional embedding, confirming earlier hints (Fig. 3A, S1H) that *Runx1*^{CKO} Ia neurons are heterogeneous. In fact, although ~71% of cells in the *Runx1*^{CKO} Ia UMAP cluster bore clean Ia identities, the rest were flagged as having mixed identity (Fig. 3C, leftmost column, row 4). Such cases of mixed neuronal profiles are unlikely to be artifacts of our analysis; algorithmic approaches did not detect any doublets in our scRNA-seq libraries (Fig. S1L–N). Rather, the mixed profiles seem to reflect incomplete conversion of a subset of SGNs to the Ia identity upon *Runx1* loss: adequate number of genes change to classify these neurons as Ia but some Ib and Ic-enriched genes are retained. While these differences could be random, an alternative possibility is that the genes that change expression play a particular role in determining specific neuronal properties.

To determine whether specific facets of SGN identities change upon *Runx1* loss, we generated four TP-RF classifiers, each based on DE gene sets limited to one of the following categories (Table S2): (1) all genes relevant for neuronal physiology (n=142); (2) genes encoding ion channels (n=67); (3) genes associated with chemical synaptic transmission (n=97); and (4) genes encoding cell adhesion molecules (n=57). After verifying robust performance of these classifiers (Fig. S2), predictions of SGN identities were generated. Classification based on genes related to neuronal physiology predicted 64% Ia, 16% Ib, and 10% Ic SGNs in the *Runx1*^{CKO} group, with 10% of total SGNs assigned a mixed identity. Within the Ia UMAP cluster, 83% of the cells were also classified as Ia in supervised classification (Fig. 3C). Classifying based on genes encoding ion channels alone produced

a similar result: 65% of total SGNs were Ia, with 82% of cells in the Ia UMAP cluster also predicted to be Ia by the TP-RF classifier (Fig. 3C). Likewise, 70% of total SGNs and 91% of cells in the Ia UMAP cluster were Ia when only genes involved in chemical synaptic transmission were considered (Fig. 3C). In contrast, only 40% of the *Runx1*^{CKO} SGNs were Ia based on cell adhesion molecules. Of the cells in the Ia UMAP cluster, 52% were assigned Ia identities by the classifier and the remainder were assigned either Ib (32%) or Ic identities (16%) (Fig. 3C). Taken together, although a large majority of SGNs in *Runx1*^{CKO} animals have typical Ia profiles, loss of *Runx1* can yield staggered gene expression outcomes in some SGNs, with more complete switchover of those related to physiological and synaptic function than to connectivity.

Effects on synaptic location and morphology

In the mature cochlea, most SGNs form a single peripheral synapse whose location on the IHC correlates with the neuron's subtype identity.[4,35] Ia SGNs make synaptic contacts on the pillar face of IHCs, while Ib and Ic SGNs innervate the modiolar face (Fig. 4A). Additionally, synapses on the modiolar side tends to have larger presynaptic ribbons[4,21,36], smaller postsynaptic glutamate receptor patches[36], and active zones where Ca^{2+} influx occurs at more depolarized potentials[37] compared to the pillar side. However, it is unclear which of these features may be dictated by SGN subtype identity. Indeed, presynaptic specializations in IHCs are influenced both by IHC-intrinsic polarity[38] and by extrinsic signals from SGNs[18] and olivocochlear efferents.[39]

We first asked whether loss of *Runx1* function results in shifts in synaptic position that match the change in proportions of Ia, Ib, and Ic SGNs revealed by scRNA-seq profiles (Fig. 2). Despite drastic reductions in Ib/Ic identities, the overall number of synapses onto IHCs was not decreased in *Runx1*^{CKO} animals compared to controls (Fig. 4B, 4C, S3A; see Methods). In fact, a modest increase in total synapse number per IHC was observed (Fig. 4C, Control:13.4±3.9; Runx1^{CKO}:15.8±3.0; Wilcoxon Rank Sum Test, p=0.006). Additionally, even though Ia SGNs were gained at the expense of Ib and Ic SGNs, the proportion of synapses on the modiolar side in *Runx1*^{CKO} mice remained unchanged (Fig. 4B,D), indicating that synapse location was unaffected (Control: 0.61±0.19; Runx1^{CKO}: 0.65±0.15; t-test, p=0.26).

To determine whether synaptic morphology tracks with SGN identity independent of location, we analyzed the volumes of glutamate receptor (GluA2) densities on each side of the IHC (Fig. S3A). In control animals, mean GluA2 volumes for individual IHCs showed a clear trend toward larger sizes on the pillar compared to the modiolar side (Fig. 4E) consistent with previous reports[21,36]. In *Runx1*^{CKO} cochleae, this difference disappeared, owing to a shift toward larger GluA2 volumes on the modiolar side (Fig. 4E,F). Two-dimensional representations of modiolar and pillar GluA2 volumes for individual IHCs revealed a distribution below the line of identity in scatter (Fig. S3B) and density plots (Fig. 4F) for control animals, indicative of a pillar-modiolar gradient. However, in *Runx1*^{CKO} animals, mean GluA2 volumes shifted closer to the line of identity, indicating weakening of the gradient. This held true even when we measured the GluA2 gradient by calculating the modiolar:pillar volume ratio on an IHC-by-IHC basis: the mean ratio was well below

0.62±0.08 in control animals but increased to 0.75±0.06 in *Runx1*^{CKO} animals (Wilcoxon Rank Sum Test, p=0.036; Fig. 4G). Thus, *Runx1* mutant SGN terminals on the modiolar side exhibited features normally associated with Ia SGN terminals on the pillar side.

Since previous studies reported opposing gradients of postsynaptic GluA2 and presynaptic ribbon volumes at IHC-SGN synapses[21], we wondered whether presynaptic changes follow shifts in GluA2 size distribution. Importantly, IHCs do not express *Runx1*[40,41] and are not targeted by *bhlhe22*^{Cre},[42] so in the cochlea of *Runx1*^{CKO} animals, direct genetic perturbation is restricted to SGNs. Presynaptic ribbon sizes, measured as mean volumes of anti-CtBP2 stained puncta, tended to be larger on the modiolar side than those on the pillar side in control animals (Fig. 4H), consistent with previous reports.[4,21] This difference disappeared upon loss of *Runx1* expression in SGNs (Fig. 4H,I); both pillar and modiolar ribbon volumes in *Runx1*^{CKO} animals matched the size distribution of pillar-localized ribbons from control animals (Fig. 4H). Two-dimensional scatter (Fig. S3C) and density plots (Fig. 4I) of modiolar vs. pillar ribbon volumes for individual IHCs revealed a distribution above the line of identity for control animals, indicative of a modiolar-pillar gradient. However, in *Runx1*^{CKO} animals, the ribbon volume distribution lay below the line of identity, indicating collapse of the gradient. This interpretation was also supported by measurements of the modiolar:pillar volume ratio per IHC: the mean modiolar:pillar ratio was 1.21±0.11 in control animals but significantly lower (0.90±0.04) in *Runx1*^{CKO} animals (Wilcoxon Rank Sum Test, p=0.028, Fig. 4J). Furthermore, we noted that IHC-to-IHC variation in mean ribbon sizes is larger on the modiolar side in the control group (see gray line and inset in Fig. 4H), suggesting that the extent of morphological heterogeneity is a distinguishing feature of these two presynaptic domains. This variation in the volume of modiolar ribbons was lost in *Runx1*^{CKO} animals, with more homogeneous size distribution akin to those on the pillar side (inset in Fig. 4H).

Thus, upon deletion of *Runx1*, both pre- and post-synaptic elements of IHC-SGN synapses changed such that size gradients collapsed and modiolar synapses became morphologically indistinguishable from pillar synapses. In addition, all the changes occurred in a direction that produced a final outcome matching the morphology of pillar synapses in control animals. Taken together, a broad shift toward Ia molecular identity in *Runx1*^{CKO} animals was accompanied by congruent changes in pre- and post-synaptic components toward Ia-specific features, even as synaptic location remained unaltered.

Neural response with altered SGN subtype census

Our studies suggest that there are more neurons with Ia-specific (high-SR like) properties in *Runx1*^{CKO} animals, notably based on expression of functionally relevant genes. Therefore, we set out to characterize SGN function in these animals by performing auditory brainstem response (ABR) recordings. Peak 1 (P1, arrow in Fig. 5A) in an ABR waveform corresponds to the composite neural activity of all SGNs.[43] Since high-SR fibers have relatively larger and more synchronized onset responses than low-SR fibers,[44] they contribute more to ensemble neural potentials like the ABR. Comparison of ABR P1 amplitude thus offers a window into changes in SGN subtype composition. For instance, loss of low-SR SGN

connectivity peripherally due to noise exposure reduces suprathreshold P1 amplitudes without affecting ABR threshold.[8,45]

ABR recordings (Fig. 5A, S4) revealed normal thresholds in *Runx1*^{CKO} mice compared to controls when tested with 5.66, 8, 11.33, 16, 22.65 and 32 kHz pure-tone bursts (Fig. 5B, Table S4). However, P1 amplitudes at suprathreshold sound pressure levels were larger, reflecting enhanced neural responses, at level-matched stimulus presentations in *Runx1*^{CKO} animals (Fig. 5A,D, Table S4). This translated to steeper growth functions in *Runx1*^{CKO} compared to littermate controls, with slope increases ranging from 1.5 to 2.7-fold (Fig. 5D). Differences were observed across the tonotopic axis, but the strongest effect was observed in mid-cochlear regions. Indicators of hair cell function were unaffected, with no detectable change in DPOAE threshold (Fig. 5C) or summating potential (arrowhead, Fig. 5A). Thus, the observed change in auditory nerve responses is likely due to altered SGN properties. These data show that the molecular changes in gene expression have functional consequences, with an expansion of SGNs with Ia identity resulting in ABR responses predicted for a cochlea with more high-SR SGNs.

Change in SGN identity upon postnatal loss of Runx1

Although molecularly distinct immature SGNs are present by late embryogenesis, perturbation of pre-hearing activity can redirect Ib and Ic SGNs towards the Ia fate.[4,6] Since a similar phenotype occurs in *Runx1*^{CKO} animals, we wondered whether *Runx1* also influences this latent capability for postnatal plasticity in SGNs.

Fate-mapping studies support the idea that SGN subtype identity remains flexible shortly after birth. *Runx1*^{CreER}*/; Ai14*/+ mice were given Tamoxifen at P1–P3, and then tdTomato+ SGNs were harvested and profiled by scRNA-seq at P27-P29 (Fig. 6A). Since *Runx1* expression is already restricted to Ib and Ic SGN precursors before birth[19,20], this fate-mapping strategy should tag neurons that have begun to take on Ib/Ic-specific molecular profiles. We found that while many neonatal *Runx1*+ SGN precursors do indeed acquire a Ib/Ic identity, Ia identities are also possible. Unsupervised clustering analysis revealed that SGNs that expressed *Runx1* at P1–P3 (and are therefore tdTomato+) can become any of the 3 subtypes of Type I SGNs (Fig. 6B). However, nearly 80% of *Runx1*-expressing SGNs retained their tentative Ib and Ic identities while the rest switched to Ia identity (Fig. 6D). Thus, although SGNs are molecularly distinct at P3, these identities can still change, consistent with previous reports that cochlear activity influences SGN subtype proportions.[4,6]

To test whether maintenance of Runx1 is a key step in the consolidation of Ib/Ic SGN identity, we ablated *Runx1* postnatally (P1–P3) in *Runx1*^{CreER}/*Runx1*^{F};*Ai14*/+ animals ("*Runx1*^{iCKO}"). Indeed, this perturbation fundamentally changed the fate outcome of SGNs: despite having intact *Runx1* expression up to P3—and being destined to retain Ib/Ic identity with ~80% probability as described above—nearly half of the *Runx1*^{iCKO} SGNs shed their Ib/Ic identities and instead become Ia SGNs, as assessed by scRNA-seq of tdTomato+ SGNs (Fig. 6C,D). This represents a nearly 150% increase in the probability of becoming a Ia SGN compared to controls. The decrease in probabilities of retaining Ib and Ic identities are

62% and 74%, respectively. Notably, 27% of *Runx1*^{iCKO} SGNs acquire 'mixed' identities. Closer examination of genes expressed in this subgroup of mutant SGNs revealed that the mixture of identities is a result of failure to shed Ic gene signatures despite having acquired Ia gene profiles (Fig. 6E,F). For example, *Runx1*^{iCKO} SGNs expressed *Rxrg*, *Calb2*, *Btbd9* and *B3gat1* at levels typical of control Ia SGNs, but failed to turn off the Ic-specific markers *Lypd1* and *Grm8*. These differences are unlikely to be driven by clustering-associated artifacts because examination of population-wide gene expression trends revealed increased representation of Ia-associated genes and decreased expression of Ib/Ic-associated genes (Fig. 6G). These findings show that Runx1 also acts postnatally to steer differentiating SGNs away from the Ia identity.

Consistent with scRNA-seq results, similar changes in SGN identity were observed using RNAscope in tissue sections of the cochlea. Most neurons that were tagged with tdTomato—indicating that they expressed *Runx1* before P3—went on to become *Calb2*^{LOW} Lypd1^{ON} (Ic) or *Calb2*^{MID}Lypd1^{OFF} neurons (Ib) in mature animals (Fig. 6H,I). In contrast, ablation of *Runx1* expression shortly after birth resulted in fewer tdTomato+ cells expressing *Lypd1* and more with higher *Calb2* levels (Fig. 6I). Indeed, tdTomato+ SGNs frequently expressed high *Calb2* levels and a subset even co-expressed *Calb2* and *Lypd1*; both of these expression patterns were rare in the control group (Fig. 6H,I). Thus, SGN identities are malleable postnatally and maintenance of Runx1 is required for final consolidation of subtype identity.

Discussion

Across sensory modalities throughout the animal kingdom, sensory neurons with heterogeneous properties encode complex stimuli. In contrast to the stark molecular differences that distinguish fundamentally different neuron types, such as excitatory and inhibitory neurons, molecular variation within a sensory neuron population is subtler and is layered on top of shared programs of gene expression. Here, we show that sensory neurons in the cochlea (i.e., SGNs) acquire subtype-specific properties through flexible use of an intrinsic transcriptional template. The key player is the TF Runx1, which coordinates broad transcriptional changes such that SGNs take on Ib or Ic identities rather than Ia identities. These molecular changes were accompanied by predicted changes in synaptic heterogeneity and in physiological responses, but not in synaptic position. Although loss of *Runx1* often led to a complete identity switch, some SGNs showed stronger changes in subtype-specific genes related to neuronal function than those that encode cell adhesion molecules, indicating that identity-related genes may be controlled hierarchically. Consistent with the fact that changes in cochlear activity can alter SGN subtype proportions, Runx1+ progenitors are not fully committed to the Ib/Ic identity and can switch to Ia identity upon loss of Runx1 just after birth. Thus, the final proportion of SGN subtypes may be shaped by an intersection between activity and Runx1's intrinsic ability to endow Ib and Ic SGNs with properties needed for encoding sound.

Our data support the idea that Runx1 is a molecular switch that promotes Ib and Ic identities while simultaneously repressing Ia identities. As assessed by both supervised and unsupervised analysis of gene expression, embryonic loss of *Runx1* creates an excess of Ia SGNs, a result that would not be possible if those cells simply lost expression of

Ib/Ic-enriched genes without gaining Ia-specific signatures. One interpretation is that Runx1 directly activates genes associated with Ib/Ic identities and directly represses those that confer Ia identity. Such a capacity to orchestrate cellular identity via both positive and negative regulation of gene expression is not unprecedented for Runx1.[22] It is also possible that Runx1 acts indirectly through expression of an as-yet unidentified intermediate TF that controls Ia identity. A thorough understanding of gene regulatory networks governing SGN identities will require additional transcriptome-level analysis of mutant mouse models, particularly at embryonic stages. Indeed, two recent studies[46,47] have reported restriction of *Runx1* expression coincident with the appearance of distinct Ic or Ib/Ic transcriptomic identities during embryogenesis, consistent with our findings. These studies may also open doors to additional, deeper inquiries into factors that drive SGN differentiation trajectories, including those that further diversify Ib and Ic lineages from a common Runx1dependent population.

Growing evidence indicates that neuronal identity is established in a sequential and modular fashion that includes early acting master regulators, intermediate switches such as Runx1, and late acting terminal selectors, which are TFs that induce and maintain specific batteries of genes needed for mature function.[15,48] Gata3[16], Neurod1[49] and Isl1[50] likely act early to shape shared SGN properties, including their basic wiring. In contrast, Runx1's effects on SGN diversification may be carried out through the action of terminal selector-like TFs that dictate different subtype-specific features. For instance, Mafb seems to control postsynaptic differentiation without affecting intrinsic firing properties,[17] whereas Pou4f1 is important for different SGN subtypes to instruct appropriate pre-synaptic differentiation in the IHC.[18] Our characterization of pre- and post-synaptic properties, synapse location as well as neural response to sound upon loss of *Runx1* serves as a valuable platform upon which the TF regulatory logic of SGN diversification can be further studied.

Although SGN identity and auditory function were dramatically altered in *Runx1*^{CKO} mice, some SGNs were only partially converted, suggesting that other factors influence Runx1's effects on gene expression. With both embryonic and postnatal deletion of *Runx1*, many cells seemingly shed their Ib/Ic identities—and became clean Ia's —even as others held on to parts of them. Why Ib/Ic gene retention occurs only in a subset of cells is not clear. Likewise, it is curious why Ib and Ic SGNs still exist among the profiled population in *Runx1*^{CKO} and *Runx1*^{iCKO}. This may be explained in part by escape from Cre-induced recombination in some SGNs (Fig. S1A). Whether cells with mixed identities represent a subgroup that are inherently less plastic and how they may be distributed along the cochleotopic axis, which contains a gradient of cellular maturation, are intriguing questions for future studies. It is also possible that cells with mixed or unaltered identities were in a more differentiated state at the time of *Runx1* loss than those that fully converted, or that activity-dependent processes impact sensitivity to Runx1. Regardless of how Runx1 activity is modulated, our data suggest that there is a hierarchy of biological features with some locked in place early while others remain amenable to change. The rigidity in expression of cell adhesion molecule-associated genes implies that SGN connectivity is more stable than functional properties through early development. Consistent with this idea, synaptic location along the basal pole of IHCs remained unaltered despite an overabundance of Ia SGNs in *Runx1*^{CKO} animals. Whether this principle also applies to subtype-specific

SGN connectivity in the cochlear nucleus is unknown. Furthermore, implications of such a heterogeneous transcriptional regulatory landscape, featuring rigidity and flexibility in expression across different gene families, remain to be elucidated.

The discovery that SGNs can switch identity without obvious changes in synapse number or position indicates that mechanisms other than circuit rewiring contribute to developmental plasticity. Throughout the nervous system, neural connections established early in life are subject to change: some are pruned while others are consolidated to yield mature neural circuits. Anatomical refinement of juvenile circuits depends critically on spontaneous or sensory input-driven neural activity.[51–54] In addition to influencing the pattern of synaptic connections, activity can also alter the functional architecture of neural circuits by shaping cell identities.[4,55] Our data underscore the presence also of stable circuits with flexible physiology in the developing nervous system. Further, we found that molecularly distinct precursors can switch developmental trajectories postnatally and introduce Runx1 as a mediator of this switch. In the somatosensory system, developing primary neurons also go through transient stages and then commit to specific subtype identities by maintaining expression of key TFs in response to target-derived cues.[56] Thus, activity-induced changes in functional identity may be a broadly active mechanism used to fine-tune circuit organization, perhaps adjusting subtype proportions based on the needs of an animal.

Given their disproportionately large number of Ia SGNs, *Runx1*^{CKO} animals are a valuable model for understanding the significance of SGN diversity for sound encoding. Although significant insights have been gained from animal models with depletion of Ic SGNs due to noise exposure or old age, *Runx1*^{CKO} animals offer the opportunity to investigate how stimulus coding changes when the neurons are predominantly of one functional class without reducing the total neuron number and outside the context of an injury model. The discovery that responses to suprathreshold stimuli are larger and grow faster emphasizes the fact that most SGNs in *Runx1*^{CKO} animals are functionally behaving like low-threshold Ia neurons. Thus, further analysis of these animals can reveal how such a change in neuronal composition impacts the animal's perception of sound. Since loss of Ic SGNs is predicted to make it harder to hear in noisy environments, the postnatal malleability of SGN identity raises the possibility of using Runx1 to restore SGN diversity and hence mitigate the effects of age-related hearing loss.

Limitations of the study

Although our results demonstrate that Runx1 contributes to SGN diversity by specifying Ib/Ic SGN identities, a small number of Ib/Ic SGNs in *Runx1*^{CKO} animals persist, possibly due to incomplete deletion of Runx1. Recombination or depletion of functional Runx1 protein might also have occurred asynchronously in *Runx1*^{CKO} SGNs, thereby generating both clean Ia and mixed identities. Finally, we focused on how heterogeneous *Runx1* expression relates to the emergence of SGN molecular diversity during late embryogenesis, and our experiments do not permit any inference regarding Runx1 expression and function immediately after SGNs become postmitotic, which commences in the cochlear base around E9.[57]

STAR Methods

RESOURCE AVAILABILITY

Lead contact—Further information and requests for resources and reagents should be directed to and will be fulfilled by the lead contact, Lisa Goodrich (Lisa_Goodrich@hms.harvard.edu).

Materials availability—This study did not generate new unique reagents.

Data and code availability—Raw scRNA-seq data generated in this study, processed gene expression matrices, and related metadata have been deposited at the NCBI Gene Expression Omnibus (GEO) repository with accession numbers GSE210215 and GSE210216. Custom R scripts are available on GitHub. Any additional information required to reanalyze the data reported in this work is available from the Lead Contact upon request.

EXPERIMENTAL MODEL AND SUBJECT DETAILS

Mice were handled and housed in accordance with standards and guidelines set by the Institutional Animal Care and Use Committees (IACUC) at Harvard Medical School. Animals of both sexes were used. No analysis was performed to determine the influence or association of sex on the results of the study. Animal genotype and age are reported where applicable, including the Key Resources Table.

METHOD DETAILS

Histology, immunohistochemistry and *in situ* gene expression analysis— Embryonic heads were promptly collected after euthanasia of the pregnant dam by CO_2 overexposure and drop-fixed in 4% paraformaldehyde (PFA) in 1x PBS. Animals older than P21 were anesthetized via isoflurane exposure by the open-drop method and perfused with 4% PFA in 1x PBS. Both cochleae were dissected out from the temporal bones and cochleostomy was performed using the tip of a scalpel blade at the basal turn to facilitate PFA entry into the cochlea. For tissues used for *in situ* hybridization assays, post-fixation was performed at 4°C for 2 hr before decalcification in 120 mM EDTA in 1xPBS for 48–72 hr at 4°C. They were then equilibrated in increasing sucrose concentrations at 4°C before cryopreservation and sectioning. For tissues used for synapse staining in whole mount preparations, post-fixation was performed for 1 hr at RT, followed by decalcification in 120 mM EDTA in 1xPBS for 48–72 hrs at 4°C. Cochlea were then micro-dissected into apical, middle, and basal turns. Following sucrose permeabilization with a freeze-thaw cycle in 30% m/v sucrose in 1x PBS, non-specific expression was blocked with blocking solution (5% v/v normal donkey serum, 5% v/v normal goat serum, and mouse fab fragments) for 1 hr. Tissues were permeabilized with 1% Triton-X in 1x PBS (PBST). Cochlear turns were stained overnight with antiPvg, anti-CtBP2, anti-GluA2, and anti-Myosin-VIIA and subsequently in appropriate secondary antibodies, both at 37°C. Rinses after primary and secondary antibody incubations were done using 1% PBST every 15 mins for 1 hr at RT.

Anti-HuD staining for assessing SGN density was done using a standard immunohistochemistry protocol as described previously (Shrestha et al, 2018) but with the

following addition: at the start of the protocol, sections were post-fixed in 4% PFA for 10 min, rinsed with 0.02% PBST, treated with Type III protease (ACD) for 10 min, rinsed in 0.02% PBST for 5 min, then blocked in consecutive 30 min segments each using 5% normal donkey serum and Fab fragments before proceeding with primary antibody incubation.

For mRNA detection by RNAscope (Advanced Cell Diagnostics), the manufacturer's protocol was used with the exception that at the end of the protocol, tissues were stained overnight with anti-HuD to mark cell bodies and incubated in the appropriate secondary antibodies for 2 hr at RT the next day. In some cases, tissues were also stained overnight with anti-dsRed to amplify endogenous tdTomato signal.

In experiments involving fate-mapping of SGNs expressing *Runx1* embryonically, a single dose of Tamoxifen (120 mg/kg body weight) was administered to pregnant *Runx1*^{CreER}/+; Ai3/+ dam to induce recombination at E15.5.

Transcriptomic profiling—Mice of both sexes and the following genotypes were used: *bhlhe22*^{Cre}/+; Ai14/+ (control) and *bhlhe22*^{Cre}/+*; Ai14*/+*; Runx1*$^{F/F}$ (*Runx1*^{CKO}) mice aged P30-P33 for scRNA-seq reported in Figures 2 and 3, and *Runx1*^{CreER}/+; Ai14/+ (control) and *Runx1*^{CreER}/*Runx1*^{F}; Ai14/+ (*Runx1*^{iCKO}) mice aged P27-P29 for scRNA-seq reported in Figure 6. A single Tamoxifen dose (120 mg/kg body weight) was administered intragastrically to neonatal mice bearing the *Runx1*^{CreER} transgene to induce recombination. SGNs were dissociated for single cell transcriptomic profiling as follows: cochleae were extracted from euthanized mice and dissected in chilled Leibovitz's L-15 buffer containing 30 uM Actinomycin D (ActD). They were then treated with collagenase type IV, followed by papain, both in the presence of 15 μM ActD, for 20 minutes each at 37 °C. Papain was inactivated by passing the cells through ovomucoid as recommended for the Papain Dissociation System (Worthington). Dissociated cells were resuspended in chilled 1x PBS containing 0.01% BSA and passed through a 35 μm filter to remove cell clumps and undigested tissue. The cell suspension thus obtained was loaded onto a MoFlo Astrios EQ Cell Sorter (Beckman Coulter) equipped with a 100 μm nozzle and 561 nm laser to enrich for tdTomato+ cells. Depending on recovery rate, 3000 to 6000 tdTomato+ cells were loaded along with appropriate Chromium Single Cell 3' reagents (v3) per well of a Chromium Chip B and processed using a 10x Chromium Controller following manufacturer recommendations within 30 minutes of completion of FACS enrichment. cDNA was amplified via 13 PCR cycles in a BioRad C1000 thermocycler. cDNA libraries containing standard P5 and P7 Illumina paired-end constructs were sequenced in an Illumina NextSeq 500 platform using a 75-cycle high-output kit. Each run of the 10x Chromium Controller consisted of a control and a Runx1^{CKO} sample, each loaded on a separate well. These samples were processed separately until library preparation but pooled for sequencing.

Image acquisition—Tissues probed by *in situ* hybridization and immunohistochemistry assays were imaged using a Leica SP8 point-scanning confocal microscope equipped with HyD and photomultiplier tube (PMT) detectors. RNAscope signals were captured with PMT detectors while immunostained cytoplasmic markers (HuD, tdTomato or YFP) were imaged with HyD or PMT detectors, both using 63x oil-immersion objective at 0.180 micron/pixel *xy* resolution. Whole-mount preparations used for synapse analysis were imaged using

PMT detectors and 63x oil-immersion objective (voxel size = 0.901 × 0.901 × 0.299 μm^3). Frequency maps were generated based on low-magnification views of cochlear pieces using the Measure_Line plugin available through the Histology Core at Mass Eye and Ear (Boston, USA). Care was taken not to oversaturate any fluorescent signal intended to be used for intensity-based morphometric quantification. Fluorescent signal meant for generating cell segmentation masks (i.e., hair cell or SGN cytoplasmic markers) were intentionally oversaturated; this was necessary to capture the full volumes of respective cells by compensating for the tendency of the software to draw cell surfaces inside actual cell boundaries.

Auditory Brainstem Responses (ABR) and Distortion Products Otoacoustic Emissions (DPOAE)—Mice were anesthetized with an intraperitoneal injection of ketamine (100 mg/kg) and xylazine (7.5 mg/kg) and placed on a 37 °C heating pad for the duration of experiment. Acoustic stimuli were delivered via a custom acoustic system from the Eaton-Peabody Lab (acoustic assembly and custom Labview software available from the Engineering Core of the Eaton-Peabody Laboratories at Massachusetts Eye and Ear, Boston) in a sound-attenuating, electrically shielded room. A dorsoventral incision at the intertragal notch of the pinna exposed the ear canal.

Distortion Product Otoacoustic Emissions (DPOAEs) were recorded for primary tones (frequency ratio $f_2/f_1 = 1.2$, level ratio $L_1 = L_2 + 10$), where f_2 varied from 5.6 to 32 kHz in half-octave steps and incremented in 10 dB steps from 10 dB to 70 dB. The cubic distortion product $2f_1\text{-}f_2$ was extracted by Fourier analysis of the ear-canal sound pressure after waveform and spectral averaging. DPOAE threshold was defined as the f_1 level required to produce a DPOAE of 0 dB SPL.

Auditory brainstem responses (ABRs) were recorded via three subdermal needle electrodes: (1) reference electrode placed caudal to the pinna, (2) active electrode in the vertex, and (3) ground electrode near the tail. Stimuli were 5-ms tone-pips with 0.5ms rise-fall time at frequencies from 5.66–32 kHz delivered in non-alternating polarity at 30 s^{-1}. Stimulus levels (SPL) were incremented in 5 dB steps from 30 dB to 80 dB. Cochlear Function Test Suite (CFTS) software (v2.19; Massachusetts Eye and Ear, Boston) amplified ($x10^4$), filtered (0.3–3 kHz passband), and averaged with 512 responses at each SPL.

QUANTIFICATION AND STATISTICAL ANALYSIS

All statistical analysis was done in R. For comparing two independent groups, normality of data distribution within each group was assessed by the Shapiro-Wilk test. If both groups showed normal distribution, Welch's t-test was performed. Otherwise, the non-parametric Wilcoxon Rank Sum Test or Kolmogorov-Smirnov (KS) Test was applied. Data are presented as mean±SD unless noted otherwise.

Bioinformatic analysis—Sequenced reads were demultiplexed to separate by experimental group and aligned to the mouse reference genome (mm10) in a Linux-based high-performance computing cluster at Harvard Medical School. Bioinformatic analysis was performed using custom scripts that utilized Seurat[58] for preliminary processing and various other packages for statistical analysis and graphical representation in the R environment.

Principal component analysis (PCA), UMAP embedding, and graph-based clustering were all performed within the Seurat environment.

Quantification of reads mapping to exon 4 of *Runx1* was done by: 1) aligning raw reads from scRNA-seq assays to a custom reference genome containing only *Runx1* exon sequences; 2) filtering the resulting binary alignment map (BAM) to retain only SGNs that passed quality-control filters and were included in cell type classification in other parts of our study (Fig. 2); 3) loading all BAM files for each genotype to generate aggregate read coverage tracks in Integrated Genomics Viewer (The Broad Institute, v2.15.2).[59]

Supervised classification was performed using SingleCellNet.[60] Ensemble learning-based approaches coerce cells, by design, into one of several possible classes present in training data (i.e., control SGNs), so cases of mixed or unresolved identities absent in the wildtype state are missed. To get around this, a 4th cell class was created by randomly permuting gene expression across all three Type I SGN subtypes, thereby creating a synthetic identity. Any cell that either matched this mixed cell class or exhibited poor resemblance (<50%) to the other pure cell classes were assigned this mixed identity. For supervised classification based on gene subsets, DE genes (among Ia, Ib and Ic SGNs in the Control group) that belonged to the following Gene Ontology groups were used: Functionally relevant (GO:0005216 & GO:0007268), Ion channel (GO:0005216), Chemical synaptic transmission (GO:0007268). List of DE genes of the cell adhesion molecule (CAM) family were drawn using those identified as CAM genes previously.[61]

Doublets were detected using the DoubletFinder[62] package in R which injected artificial doublets into our dataset at a set proportion and subsequently defined each SGN's neighborhood in gene expression space. Optimal pK value was determined by BC_{MVN} (mean-variance-normalized bimodality coefficient) maximization: the pK parameter was varied over a range before picking one that yielded the highest BC_{MVN} (Fig. S1L). Finally, the proportion of artificial nearest neighbors (pANN) was calculated (Fig. S1M). Cells with the highest pANN values were deemed to be doublets as described previously (Fig. S1N).

Image analysis

In situ gene expression assays: Quantification of RNAscope signal in tissue sections was performed by generating counts of fluorescent puncta within SGN soma segmented based on anti-HuD in 3D confocal stacks using Imaris (v9, Oxford Instruments). Detection of genetically encoded fluorescent reporter (e.g., tdTomato, YFP) in lineage-tracing experiments was performed similarly, except the Imaris output was binarized to yield ON/OFF status for each SGN. Subsequent data processing and statistical analysis was done in the R environment.

Neuronal density in the SG: SGN density was analyzed blind to genotype by following these steps in ImageJ[63]: (1) manually counting neuronal cell bodies stained with anti-HuD in maximum intensity projections of spiral ganglia of cryosectioned cochlea; and (2) measuring ganglion area using the 'Polygon selections' tool to outline inner edge of Rosenthal's canal based on background staining by the Donkey anti-mouse secondary used against anti-HuD primary, and then applying the 'Measure' function.

Synapse count, position and morphometry: A combination of Imaris, MATLAB and R was used to analyze hair cell (HC)-SGN synapses marked by anti-CtBP2 and anti-GluA2: creation of 3D hair cell segmentation masks as well as determination of synaptic element volume and position in image-centric cartesian coordinates (Fig. 4B) was accomplished semi-automatically in Imaris. Membership of synaptic elements to particular HCs was determined automatically in Imaris based on inclusion within a segmented volume. Any Imaris-rendered HC segmentation mask meeting the following criteria were excluded from further analysis: (1) missed portions of the HC and synaptic elements associated with it; and (2) encapsulated >1 HC. References for HC-centric coordinates were then created in ImageJ by manually annotating the following landmarks as singular points in the z-stack for each HC using a custom macro: the back of the cuticular plate (i.e., the side closest to the tallest sterocilia row), the center of the nucleus, mid-point along the bottom of the hair cell. Data generated in Imaris and ImageJ were then processed using custom-written R and MATLAB scripts. Notably, image-centric coordinates (Fig. 4A) corresponding to position of synaptic elements were transformed to HC-centric coordinates (Fig. 4B) with the origin set at the base of each HC and the coordinates rotated to account for the unique tilt of each HC. The latter was achieved by aligning the y-axis of the new coordinate system with a slicer plane (Fig. S3A) that connected the mid-point at the bottom of the HC with the back of its cuticular plate (Fig. S3A, 4B). The slicer plane effectively partitioned each HC into modiolar (facing the modiolus) and pillar (facing the pillar cell) volumes, which enabled assignment of ‘modiolar’ and ‘pillar’ designations to each synaptic element based on their location within the respective volumes. To account for staining intensity variation across tissues, ribbon and glutamate receptor volumes were normalized relative to the respective median volumes in each z-stack as described previously.[36] Synaptic elements that did not have a corresponding pre- or post-synaptic element nearby was excluded from our analysis. A small subset of HCs exhibited extremely skewed distribution of modiolar and pillar synaptic elements (e.g., all elements were modiolar); these were excluded from analysis as they may represent immunostaining, slide mounting or segmentation artifacts. Statistical analysis was performed in R. All of these analyses were done blind to genotype.

Analysis of ABRs: ABR Peak Analysis software (v.1.1.1.9; Massachusetts Eye and Ear, Boston) was used to determine thresholds and measure peak amplitudes and latencies for ABRs. ABR threshold was defined as the SPL at which a reproducible response waveform appeared. Threshold, peaks and troughs were verified by blinded visual inspection. Wave amplitude was defined as the difference between the peak and subsequent trough.

Supplementary Material

Refer to Web version on PubMed Central for supplementary material.

Acknowledgments

We thank Dr. Bernardo Sabatini (Harvard) for use of the Chromium Controller, Dr. M. Charles Liberman (Massachusetts Eye and Ear, Harvard) for helpful discussions, and Drs. Gord Fishell (Harvard), Qiufu Ma (Harvard) and M. Charles Liberman for critical feedback on the manuscript. This work was supported by NIH/NIDCD grants R01DC009223 to L.V.G. and R21DC018356 to B.R.S., and a Lefler Postdoctoral Fellowship at Harvard Medical School to B.R.S.

References

1. Shrestha BR, and Goodrich LV (2019). Wiring the Cochlea for Sound Perception. In The Oxford Handbook of the Auditory Brainstem, Kandler K, ed. (Oxford University Press). 10.1093/oxfordhb/9780190849061.013.1.
2. Bharadwaj HM, Verhulst S, Shaheen L, Liberman MC, and Shinn-Cunningham BG (2014). Cochlear neuropathy and the coding of supra-threshold sound. Front Syst Neurosci 8. 10.3389/fnsys.2014.00026.
3. Rutherford MA, Gersdorff H, and Goutman JD (2021). Encoding sound in the cochlea: from receptor potential to afferent discharge. J Physiol 599, 2527–2557. 10.1113/JP279189. [PubMed: 33644871]
4. Shrestha BR, Chia C, Wu L, Kujawa SG, Liberman MC, and Goodrich L. v (2018). Sensory Neuron Diversity in the Inner Ear Is Shaped by Activity. Cell 174, 1229–1246.e17. 10.1016/j.cell.2018.07.007. [PubMed: 30078709]
5. Petitpré C, Wu H, Sharma A, Tokarska A, Fontanet P, Wang Y, Helmbacher F, Yackle K, Silberberg G, Hadjab S, et al. (2018). Neuronal heterogeneity and stereotyped connectivity in the auditory afferent system. Nat Commun 9, 3691. 10.1038/s41467-018-06033-3. [PubMed: 30209249]
6. Sun S, Babola T, Pregernig G, So KS, Nguyen M, Su S-SM, Palermo AT, Bergles DE, Burns JC, and Müller U (2018). Hair Cell Mechanotransduction Regulates Spontaneous Activity and Spiral Ganglion Subtype Specification in the Auditory System. Cell 174, 1247–1263.e15. 10.1016/j.cell.2018.07.008. [PubMed: 30078710]
7. Liberman MC (1978). Auditory-nerve response from cats raised in a low-noise chamber. J Acoust Soc Am 63, 442–455. 10.1121/1.381736. [PubMed: 670542]
8. Furman AC, Kujawa SG, and Liberman MC (2013). Noise-induced cochlear neuropathy is selective for fibers with low spontaneous rates. J Neurophysiol 110, 577–586. 10.1152/jn.00164.2013. [PubMed: 23596328]
9. Schmiedt RA, Mills JH, and Boettcher FA (1996). Age-related loss of activity of auditory-nerve fibers. J Neurophysiol 76, 2799–2803. [PubMed: 8899648]
10. Kujawa SG, and Liberman MC (2015). Synaptopathy in the noise-exposed and aging cochlea: Primary neural degeneration in acquired sensorineural hearing loss. Hear Res 330, 191–199. 10.1016/j.heares.2015.02.009. [PubMed: 25769437]
11. Costalupes J (1985). Representation of tones in noise in the responses of auditory nerve fibers in cats. I. Comparison with detection thresholds. The Journal of Neuroscience 5, 3261–3269. 10.1523/JNEUROSCI.05-12-03261.1985. [PubMed: 4078627]
12. Young ED, and Barta PE (1986). Rate responses of auditory nerve fibers to tones in noise near masked threshold. J Acoust Soc Am 79, 426–442. 10.1121/1.393530. [PubMed: 3950195]
13. Allan DW, and Thor S (2015). Transcriptional selectors, masters, and combinatorial codes: regulatory principles of neural subtype specification. Wiley Interdiscip Rev Dev Biol 4, 505–528. 10.1002/wdev.191. [PubMed: 25855098]
14. Shirasaki R, and Pfaff SL (2002). Transcriptional Codes and the Control of Neuronal Identity. Annu Rev Neurosci 25, 251–281. 10.1146/annurev.neuro.25.112701.142916. [PubMed: 12052910]
15. Hobert O (2011). Regulation of Terminal Differentiation Programs in the Nervous System. Annu Rev Cell Dev Biol 27, 681–696. 10.1146/annurev-cellbio-092910-154226. [PubMed: 21985672]
16. Appler JM, Lu CC, Druckenbrod NR, Yu W-M, Koundakjian EJ, and Goodrich LV (2013). Gata3 Is a Critical Regulator of Cochlear Wiring. Journal of Neuroscience 33, 3679–3691. 10.1523/JNEUROSCI.4703-12.2013. [PubMed: 23426694]
17. Yu WM, Appler JM, Kim YH, Nishitani AM, Holt JR, and Goodrich LV (2013). A Gata3-Mafb transcriptional network directs post-synaptic differentiation in synapses specialized for hearing. Elife, e01341. 10.7554/eLife.01341.001. [PubMed: 24327562]
18. Sherrill HE, Jean P, Driver EC, Sanders TR, Fitzgerald TS, Moser T, and Kelley MW (2019). Pou4f1 Defines a Subgroup of Type I Spiral Ganglion Neurons and Is Necessary for Normal Inner Hair Cell Presynaptic Ca^{2+} Signaling. The Journal of Neuroscience 39, 5284–5298. 10.1523/JNEUROSCI.2728-18.2019. [PubMed: 31085606]

19. Petitpré C, Faure L, Uhl P, Fontanet P, Filova I, Pavlinkova G, Adameyko I, Hadjab S, and Lallemend F (2022). Single-cell RNA-sequencing analysis of the developing mouse inner ear identifies molecular logic of auditory neuron diversification. Nat Commun 13, 3878. 10.1038/s41467-022-31580-1. [PubMed: 35790771]
20. Sanders TR, and Kelley MW (2022). Specification of neuronal subtypes in the spiral ganglion begins prior to birth in the mouse. Proceedings of the National Academy of Sciences 119. 10.1073/pnas.2203935119.
21. Liberman LD, and Liberman MC (2016). Postnatal maturation of auditory-nerve heterogeneity, as seen in spatial gradients of synapse morphology in the inner hair cell area. Hear Res 339, 12–22. 10.1016/j.heares.2016.06.002. [PubMed: 27288592]
22. Chen CL, Broom DC, Liu Y, de Nooij JC, Li Z, Cen C, Samad OA, Jessell TM, Woolf CJ, and Ma Q (2006). Runx1 determines nociceptive sensory neuron phenotype and is required for thermal and neuropathic pain. Neuron 49, 365–377. 10.1016/j.neuron.2005.10.036. [PubMed: 16446141]
23. Kramer I, Sigrist M, de Nooij JC, Taniuchi I, Jessell TM, and Arber S (2006). A Role for Runx Transcription Factor Signaling in Dorsal Root Ganglion Sensory Neuron Diversification. Neuron 49, 379–393. 10.1016/j.neuron.2006.01.008. [PubMed: 16446142]
24. Huang S, O'Donovan KJ, Turner EE, Zhong J, and Ginty DD (2015). Extrinsic and intrinsic signals converge on the Runx1/CBFβ transcription factor for nonpeptidergic nociceptor maturation. Elife 4, e10874. 10.7554/eLife.10874. [PubMed: 26418744]
25. Mevel R, Draper JE, Lie-a-Ling M, Kouskoff V, and Lacaud G (2019). RUNX transcription factors: orchestrators of development. Development 146. 10.1242/dev.148296.
26. Coate TM, Spita NA, Zhang KD, Isgrig KT, and Kelley MW (2015). Neuropilin-2/semaphorin-3F-mediated repulsion promotes inner hair cell innervation by spiral ganglion neurons. Elife 4, 1–24. 10.7554/eLife.07830.
27. Koundakjian EJ, Appler JL, and Goodrich LV (2007). Auditory Neurons Make Stereotyped Wiring Decisions before Maturation of Their Targets. Journal of Neuroscience 27, 14078–14088. 10.1523/JNEUROSCI.3765-07.2007. [PubMed: 18094247]
28. Samokhvalov IM, Samokhvalova NI, and Nishikawa S (2007). Cell tracing shows the contribution of the yolk sac to adult haematopoiesis. Nature 446, 1056–1061. 10.1038/nature05725. [PubMed: 17377529]
29. Ross SE, Mardinly AR, McCord AE, Zurawski J, Cohen S, Jung C, Hu L, Mok SI, Shah A, Savner EM, et al. (2010). Loss of inhibitory interneurons in the dorsal spinal cord and elevated itch in Bhlhb5 mutant mice. Neuron 65, 886–898. 10.1016/j.neuron.2010.02.025. [PubMed: 20346763]
30. Growney JD, Shigematsu H, Li Z, Lee BH, Adelsperger J, Rowan R, Curley DP, Kutok JL, Akashi K, Williams IR, et al. (2005). Loss of Runx1 perturbs adult hematopoiesis and is associated with a myeloproliferative phenotype. Blood 106, 494–504. 10.1182/blood-2004-08-3280. [PubMed: 15784726]
31. Wang Q, Stacy T, Binder M, Marin-Padilla M, Sharpe AH, and Speck NA (1996). Disruption of the Cbfa2 gene causes necrosis and hemorrhaging in the central nervous system and blocks definitive hematopoiesis. Proc Natl Acad Sci U S A 93, 3444–3449. 10.1073/pnas.93.8.3444. [PubMed: 8622955]
32. Tong L, Strong MK, Kaur T, Juiz JM, Oesterle EC, Hume C, Warchol ME, Palmiter RD, and Rubel EW (2015). Selective deletion of cochlear hair cells causes rapid age-dependent changes in spiral ganglion and cochlear nucleus neurons. J Neurosci 35, 7878–7891. 10.1523/JNEUROSCI.2179-14.2015. [PubMed: 25995473]
33. Pan H, Song Q, Huang Y, Wang J, Chai R, Yin S, and Wang J (2017). Auditory Neuropathy after Damage to Cochlear Spiral Ganglion Neurons in Mice Resulting from Conditional Expression of Diphtheria Toxin Receptors. Sci Rep 7, 6409. 10.1038/s41598-017-06600-6. [PubMed: 28743950]
34. Arlotta P, and Hobert O (2015). Homeotic Transformations of Neuronal Cell Identities. Trends Neurosci 38, 751–762. 10.1016/j.tins.2015.10.005. [PubMed: 26596501]
35. Liberman MC (1982). Single-neuron labeling in the cat auditory nerve. Science 216, 1239–1241. 10.1126/science.7079757. [PubMed: 7079757]

36. Liberman LD, Wang H, and Liberman MC (2011). Opposing Gradients of Ribbon Size and AMPA Receptor Expression Underlie Sensitivity Differences among CochlearNerve/Hair-Cell Synapses. Journal of Neuroscience 31, 801–808. 10.1523/JNEUROSCI.3389-10.2011. [PubMed: 21248103]
37. Ohn T-L, Rutherford MA, Jing Z, Jung S, Duque-Afonso CJ, Hoch G, Picher MM, Scharinger A, Strenzke N, and Moser T (2016). Hair cells use active zones with different voltage dependence of Ca2+ influx to decompose sounds into complementary neural codes. Proc Natl Acad Sci U S A 113, E4716–25. 10.1073/pnas.1605737113. [PubMed: 27462107]
38. Jean P, Özçete ÖD, Tarchini B, and Moser T (2019). Intrinsic planar polarity mechanisms influence the position-dependent regulation of synapse properties in inner hair cells. Proc Natl Acad Sci U S A 116, 9084–9093. 10.1073/pnas.1818358116. [PubMed: 30975754]
39. Yin Y, Liberman LD, Maison SF, and Liberman MC (2014). Olivocochlear innervation maintains the normal modiolar-pillar and habenular-cuticular gradients in cochlear synaptic morphology. JARO - Journal of the Association for Research in Otolaryngology 15, 571–583. 10.1007/s10162-014-0462-z. [PubMed: 24825663]
40. Scheffer DI, Shen J, Corey DP, and Chen Z-Y (2015). Gene Expression by Mouse Inner Ear Hair Cells during Development. Journal of Neuroscience 35, 6366–6380. 10.1523/JNEUROSCI.5126-14.2015. [PubMed: 25904789]
41. Kolla L, Kelly MC, Mann ZF, Anaya-Rocha A, Ellis K, Lemons A, Palermo AT, So KS, Mays JC, Orvis J, et al. (2020). Characterization of the development of the mouse cochlear epithelium at the single cell level. Nat Commun 11, 2389. 10.1038/s41467-020-16113-y. [PubMed: 32404924]
42. Meng X, Murali S, Cheng Y-F, Lu J, Hight AE, Kanumuri V. v., Brown MC, Holt JR, Lee DJ, and Edge ASB (2019). Increasing the expression level of ChR2 enhances the optogenetic excitability of cochlear neurons. J Neurophysiol 122, 1962–1974. 10.1152/jn.00828.2018. [PubMed: 31533018]
43. Melcher JR, and Kiang NYS (1996). Generators of the brainstem auditory evoked potential in cat III: identified cell populations. Hear Res 93, 52–71. 10.1016/0378-5955(95)00200-6. [PubMed: 8735068]
44. Bourien J, Tang Y, Batrel C, Huet A, Lenoir M, Ladrech S, Desmadryl G, Nouvian R, Puel J-L, and Wang J (2014). Contribution of auditory nerve fibers to compound action potential of the auditory nerve. J Neurophysiol 112, 1025–1039. 10.1152/jn.00738.2013. [PubMed: 24848461]
45. Kujawa SG, and Liberman MC (2009). Adding Insult to Injury: Cochlear Nerve Degeneration after “Temporary” Noise-Induced Hearing Loss. Journal of Neuroscience 29, 14077–14085. 10.1523/JNEUROSCI.2845-09.2009. [PubMed: 19906956]
46. Sanders TR, and Kelley MW (2022). Specification of neuronal subtypes in the spiral ganglion begins prior to birth in the mouse. Proceedings of the National Academy of Sciences 119. 10.1073/pnas.2203935119.
47. Petitpré C, Faure L, Uhl P, Fontanet P, Filova I, Pavlinkova G, Adameyko I, Hadjab S, and Lallemend F (2022). Single-cell RNA-sequencing analysis of the developing mouse inner ear identifies molecular logic of auditory neuron diversification. Nat Commun 13, 3878. 10.1038/s41467-022-31580-1. [PubMed: 35790771]
48. Hobert O (2016). Terminal Selectors of Neuronal Identity. In Current Topics in Developmental Biology, pp. 455–475. 10.1016/bs.ctdb.2015.12.007.
49. Macova I, Pysanenko K, Chumak T, Dvorakova M, Bohuslavova R, Syka J, Fritzsch B, and Pavlinkova G (2019). Neurod1 Is Essential for the Primary Tonotopic Organization and Related Auditory Information Processing in the Midbrain. The Journal of Neuroscience 39, 984–1004. 10.1523/JNEUROSCI.2557-18.2018. [PubMed: 30541910]
50. Filova I, Pysanenko K, Tavakoli M, Vochyanova S, Dvorakova M, Bohuslavova R, Smolik O, Fabriciova V, Hrabalova P, Benesova S, et al. (2022). ISL1 is necessary for auditory neuron development and contributes toward tonotopic organization. Proceedings of the National Academy of Sciences 119. 10.1073/pnas.2207433119.
51. Katz LC, and Shatz CJ (1996). Synaptic Activity and the Construction of Cortical Circuits. Science (1979) 274, 1133–1138. 10.1126/science.274.5290.1133.

52. Faust TE, Gunner G, and Schafer DP (2021). Mechanisms governing activity-dependent synaptic pruning in the developing mammalian CNS. Nat Rev Neurosci 22, 657–673. 10.1038/s41583-021-00507-y. [PubMed: 34545240]

53. Kirkby LA, Sack GS, Firl A, and Feller MB (2013). A role for correlated spontaneous activity in the assembly of neural circuits. Neuron 80, 1129–1144. 10.1016/j.neuron.2013.10.030. [PubMed: 24314725]

54. Leighton AH, and Lohmann C (2016). The Wiring of Developing Sensory Circuits—From Patterned Spontaneous Activity to Synaptic Plasticity Mechanisms. Front Neural Circuits 10. 10.3389/fncir.2016.00071.

55. Cheng S, Butrus S, Tan L, Xu R, Sagireddy S, Trachtenberg JT, Shekhar K, and Zipursky SL (2022). Vision-dependent specification of cell types and function in the developing cortex. Cell 185, 311–327.e24. 10.1016/j.cell.2021.12.022. [PubMed: 35063073]

56. Sharma N, Flaherty K, Lezgiyeva K, Wagner DE, Klein AM, and Ginty DD (2020). The emergence of transcriptional identity in somatosensory neurons. Nature 577, 392–398. 10.1038/s41586-019-1900-1. [PubMed: 31915380]

57. Koundakjian EJ, Appler JL, and Goodrich L. v. (2007). Auditory Neurons Make Stereotyped Wiring Decisions before Maturation of Their Targets. Journal of Neuroscience 27, 14078–14088. 10.1523/JNEUROSCI.3765-07.2007. [PubMed: 18094247]

58. Stuart T, Butler A, Hoffman P, Hafemeister C, Papalexi E, Mauck WM, Hao Y, Stoeckius M, Smibert P, and Satija R (2019). Comprehensive Integration of Single-Cell Data. Cell 177, 1888–1902.e21. 10.1016/j.cell.2019.05.031. [PubMed: 31178118]

59. Thorvaldsdóttir H, Robinson JT, and Mesirov JP (2013). Integrative Genomics Viewer (IGV): high-performance genomics data visualization and exploration. Brief Bioinform 14, 178–192. 10.1093/bib/bbs017. [PubMed: 22517427]

60. Tan Y, and Cahan P (2019). SingleCellNet: A Computational Tool to Classify Single Cell RNA-Seq Data Across Platforms and Across Species. Cell Syst 9, 207–213.e2. 10.1016/j.cels.2019.06.004. [PubMed: 31377170]

61. Földy C, Darmanis S, Aoto J, Malenka RC, Quake SR, and Südhof TC (2016). Single-cell RNAseq reveals cell adhesion molecule profiles in electrophysiologically defined neurons. Proc Natl Acad Sci U S A 113, E5222–31. 10.1073/pnas.1610155113. [PubMed: 27531958]

62. McGinnis CS, Murrow LM, and Gartner ZJ (2019). DoubletFinder: Doublet Detection in Single-Cell RNA Sequencing Data Using Artificial Nearest Neighbors. Cell Syst 8, 329–337.e4. 10.1016/j.cels.2019.03.003. [PubMed: 30954475]

63. Schindelin J, Arganda-Carreras I, Frise E, Kaynig V, Longair M, Pietzsch T, Preibisch S, Rueden C, Saalfeld S, Schmid B, et al. (2012). Fiji: an open-source platform for biological-image analysis. Nat Methods 9, 676–682. 10.1038/nmeth.2019. [PubMed: 22743772]

Highlights

- Runx1 is necessary for generation of Ib/Ic SGN subtype identities.
- Runx1 loss has broader effect on genes related to neural function than to connectivity.
- Postnatal deletion of Runx1 switches SGN identity.
- Overabundance of Ia SGNs results in enhanced auditory nerve response.

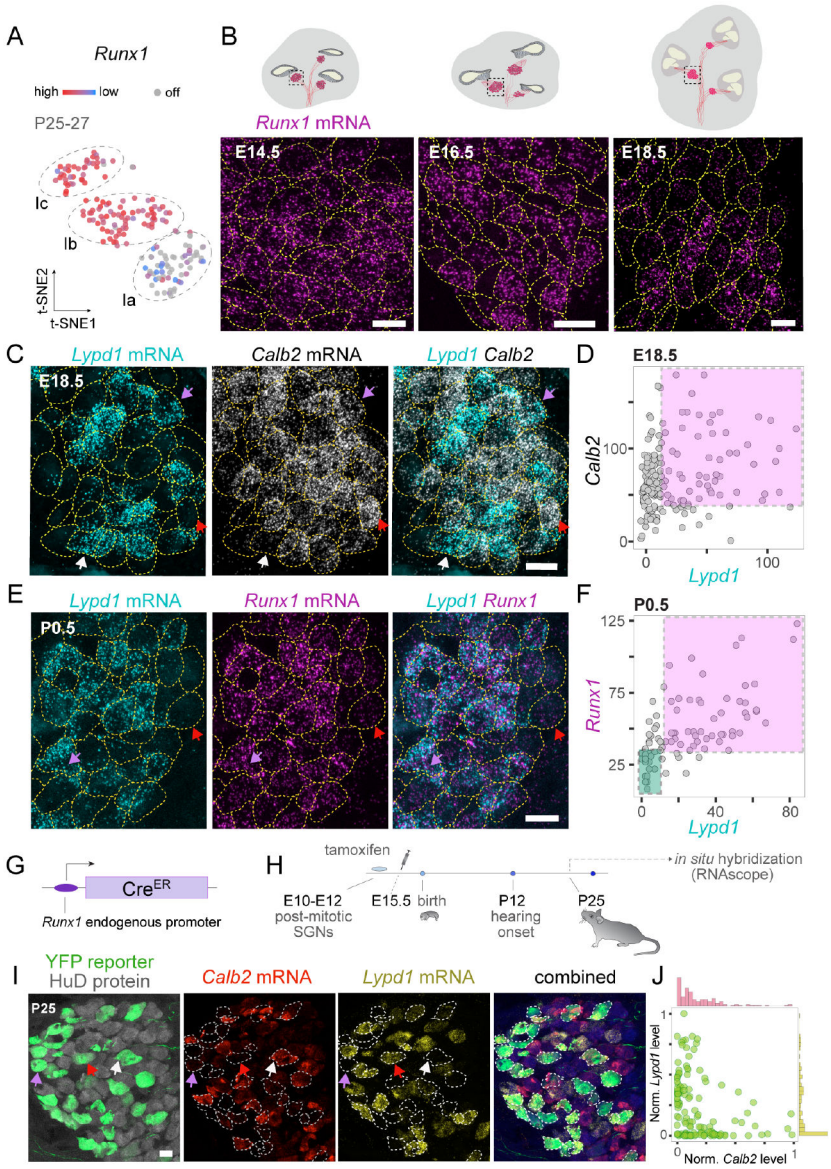

Figure 1: *Runx1* expression dynamics in SGNs tracks emergence of subtype identities

(**A**) *Runx1* is expressed in Ib and Ic neurons, as shown by t-SNE embedding of Type I SGN scRNA-seq profiles from data in Shrestha et al. (2018). (**B-F**) *Runx1, Calb2,* and *Lypd1* expression was assessed across development by RNAscope on mid-modiolar sections through cochleae of *bhlhe22-Cre/+;Ai14/+* mice. B,C,E show highmagnification views of spiral ganglia as depicted in schematics in B. **(B)** *Runx1* expression in SGNs is broad at E14.5 (left) and more restricted at E16.5 (middle). By E18.5 (right), cells with high and low levels of *Runx1* can be clearly distinguished. (**C,D**) The SGN subtype-specific markers *Calb2* and *Lypd1* exhibit restricted expression by E18.5, with the number of fluorescent puncta per SGN quantified in D. Although the *Calb2* gradient is weak, *Lypd1* expression is highly variable, with distinct *Lypd1*^{ON} and *Lypd1*^{OFF} cells (white and red arrows, respectively, C). However, some *Lypd1*^{ON} neurons co-express *Calb2* (purple arrow, C; magenta box, D), suggesting incomplete segregation at this stage. (**E**, **F**) At birth, *Runx1*

expression remains segregated and co-varies with *Lypd1*, quantified in F. Like mature Ic SGNS, neurons with high *Runx1* expression tend to be *Lypd1*^{ON} (purple arrows, E; magenta box, F, Pearson's correlation coefficient, r=0.63). *Lypd1*^{OFF} neurons express either low or no *Runx1* (red arrows, E; teal box, F), which is observed normally in mature Ib and Ia SGNs, respectively. (**G-H**) Fate mapping of Runx1^{+} cells was achieved using *Runx1*^{CreER} knock-in mice, which express CreER recombinase under regulation of the endogenous *Runx1* promoter (G). Tamoxifen was injected at E15.5 and SGN fate was assessed at P25 by RNAscope (H). (**I**) Many cells that were *Runx1*$^{+}$ embryonically went on to become Ic (*Lypd1*^{ON}, red arrows) or Ib SGNs (*Lypd1*^{OFF} with low *Calb2* expression, purple arrows). A small subset (white arrow) acquired Ia identities (high *Calb2*). HuD immunostaining (gray) marks all SGN somata. **J**) Scatterplot based on normalized *Calb2* and *Lypd1* levels in YFP^{+} SGNs, as pictured in I. Marginal histograms show distribution of SGNs across *Calb2* (red) and *Lypd1* (yellow) expression levels. Dotted lines in B, C, E, and I represent outlines hand-drawn based on expression of *bhlhe22*^{Cre}-induced tdTomato (B,C,E) or YFP (I) in SGN somata. Scale bars: 10 microns

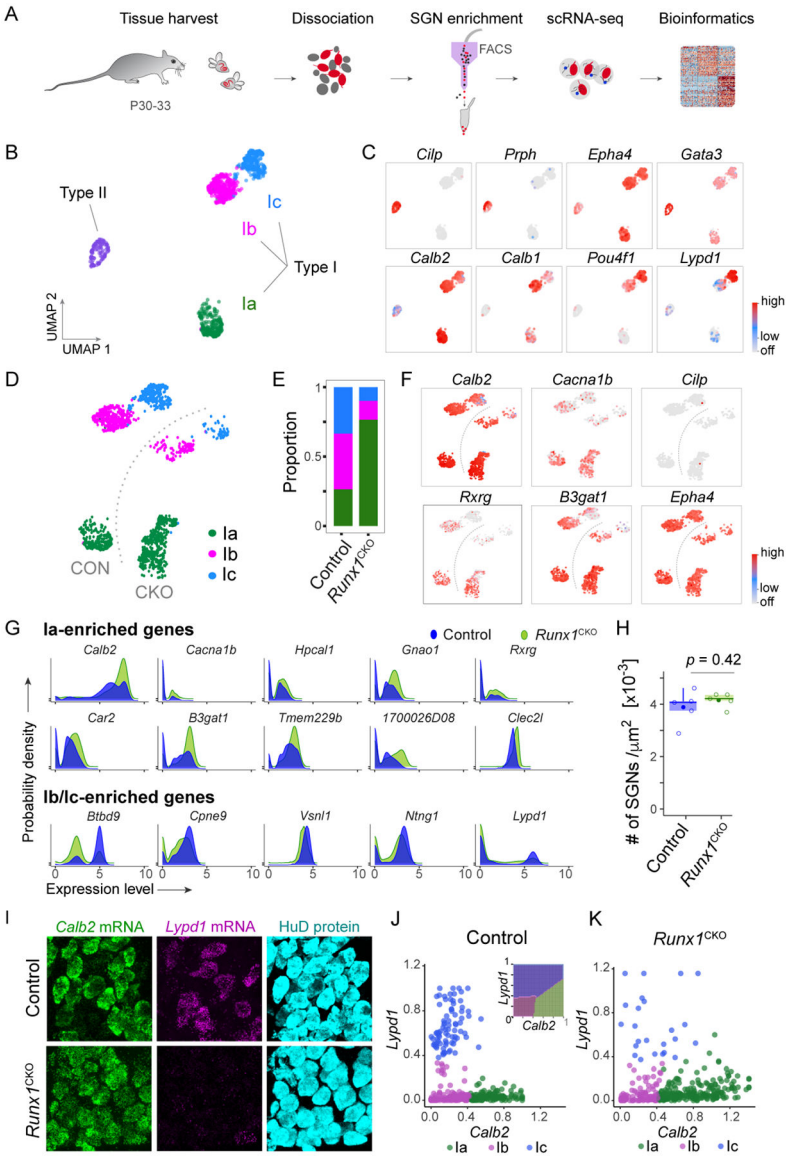

Figure 2: SGN subtype composition is altered upon loss of *Runx1* expression

(A) Our workflow for FACS-based enrichment and scRNA-seq analysis of SGNs with *bhlhe22*^{Cre}-induced tdTomato. (**B,C**) Two-dimensional embedding and unsupervised clustering of neuronal profiles from control animals revealed clusters corresponding to Ia, Ib, Ic and Type II SGNs, identified by markers shown in feature plots (C). (**D**) Three Type I SGN clusters were also identified in *Runx1*^{CKO} mice, shown in a cropped and transformed UMAP plot that excludes Type II SGNs and offsets the two genotypes for easier visualization (see Fig. S1E). (**E**) Neuronal census was drastically different, with more Ia SGNs in *Runx1*^{CKO} animals (76.6% vs 26.4% in Control) and fewer Ib (13.6% vs 40.2%) and Ic (9.7% vs 33.4%) SGNs. (**F**) The expanded pool of Ia SGNs in *Runx1*^{CKO} mice expressed Ia markers (high *Calb2*, *Rxrg*, *Cacna1b*, *B3gat1*) without any change in Type I (*Epha4*) vs. Type II (*Cilp*) markers. Cells in Ib and Ic clusters in the *Runx1*^{CKO} group did not acquire Ia markers, indicating that gain of Ia-like profiles at the expense of Ib and Ic

profiles is the key outcome of Runx1 loss. (**G**) Assessment of gene expression across the entire pool of SGNs agnostic to their identity revealed that markers known to be Ia-enriched were expressed in more *Runx1*^{CKO} mutant cells (green) compared to controls (blue). Conversely, Ib/Ic-enriched genes were underrepresented. (**H**) Cell density in the spiral ganglion was statistically identical between control and *Runx1*^{CKO} groups (t-test, p=0.42). (**I**) RNAscope-based evaluation of SGN subtype identities revealed flattened *Calb2* gradients and drastic reduction of *Lypd1*, with SGN somata visualized by HuD immunostaining. (**J**) K-means clustering of RNAscope-based molecular profiles yielded Calb2^{HI} Lypd1^{LOW} (green), Calb2^{LOW} Lypd1^{LOW} (magenta) and Calb2^{LOW} Lypd1^{HI} (blue) SGN subgroups. A support vector machine (SVM)-based classifier (inset in **J**) was generated using SGN profiles from control animals and used to predict the identities of *Runx1*^{CKO} SGNs. (**K**) This analysis revealed severe reduction in the census of Ic-like Calb2^{LOW} Lypd1^{HI} SGN profiles (blue) and expansion of Ia-like Calb2^{HI} Lypd1^{LOW} (green) identities.

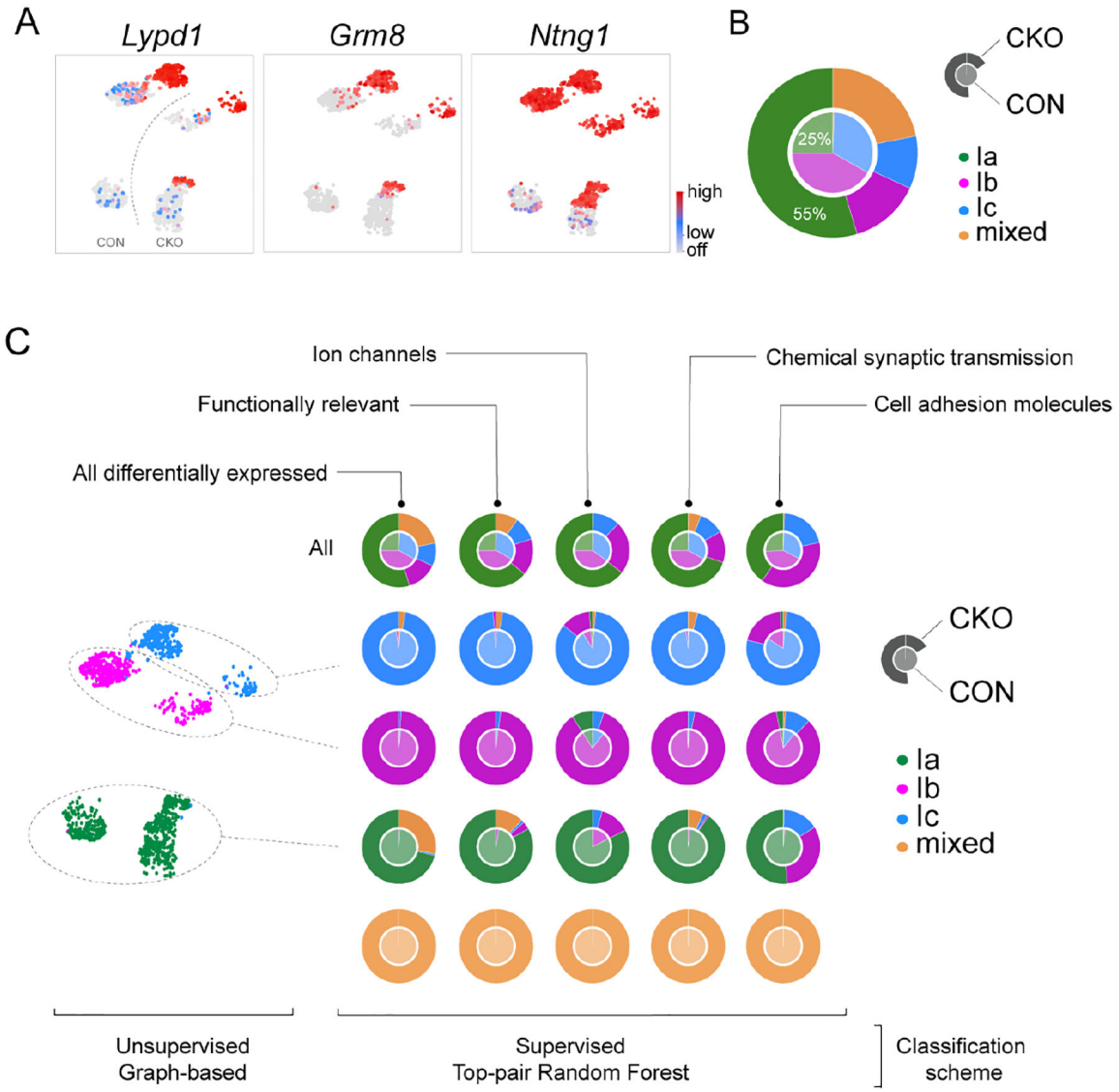

Figure 3: Varying influence of Runx1 loss on different gene categories

(**A**) Feature plots showing examples of Ic-enriched genes expressed ectopically in the *Runx1*^{CKO} Ia cluster. (**B**) SGN subtype census determined by a supervised classification scheme designed to detect unresolved or mixed identities. Outer ring represents cell proportions in *Runx1*^{CKO} and center pie represents those in Control. Ia SGNs are overrepresented in *Runx1*^{CKO} animals by 118% relative to Control, but 22% of SGNs are of mixed identity. (**C**) SGN clusters identified using an unsupervised approach were classified a second time using a supervised approach with different gene sets. Rows correspond to the subsets of SGNs that underwent supervised classification and the columns indicate gene subsets used for that analysis. Bottom row (yellow) shows how the classifier performed at detecting synthetically created mixed identities spiked into the training dataset. Supervised classification taking all genes differentially expressed among Ia, Ib, and Ic Control SGNs (leftmost column) showed that the vast majority of mixed identity SGNs are from the Ia cluster in the UMAP plot. Results of supervised classification using gene subsets drawn

from different ontological groups are shown in columns 2–5. More *Runx1*^{CKO} Ia SGNs were assigned Ib (magenta) and Ic (blue) identities when only cell adhesion molecules were used for classification (rightmost column) than when the gene set encoded functionally relevant proteins, ion channels, or chemical synaptic transmission components.

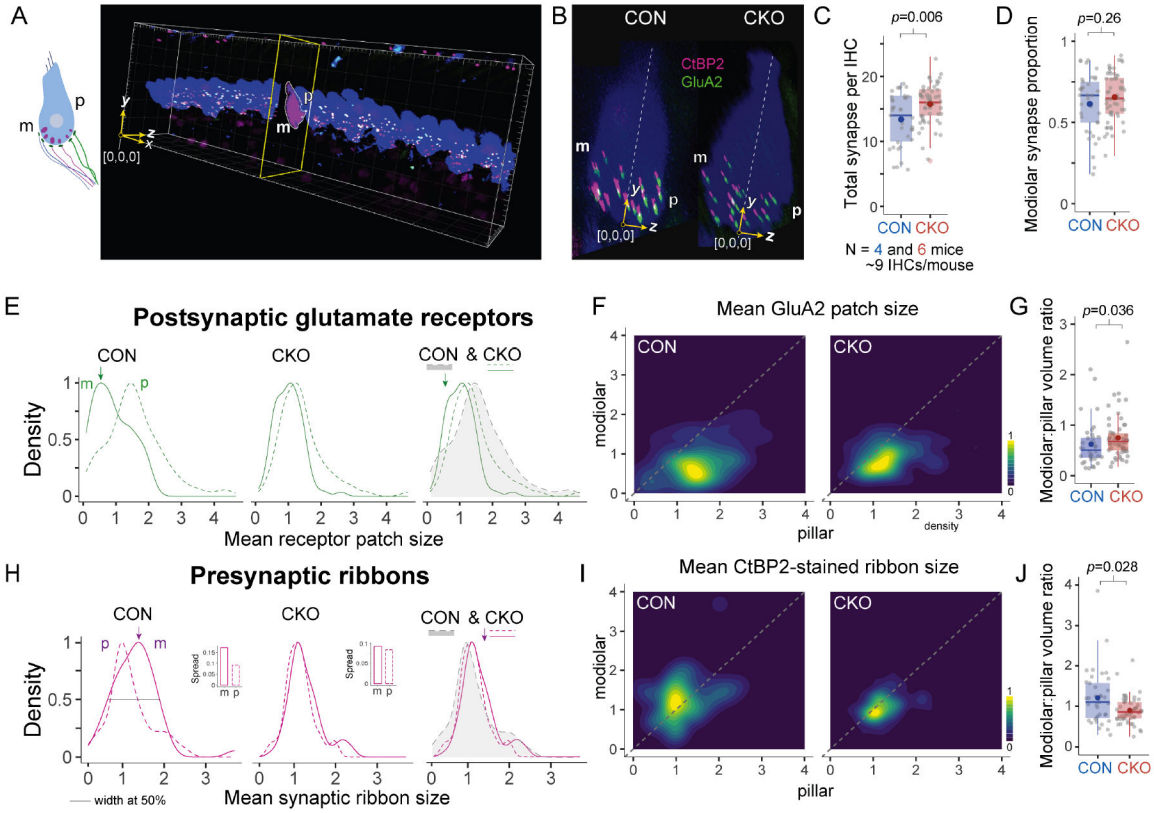

Figure 4: Change and stability in synaptic properties with *Runx1* loss

(**A,B**) Ia, Ib, and Ic SGN terminals are arranged along the pillar (p) to modiolar (m) axis of the inner hair cell (IHC). Cochlear wholemounts were immunostained for CtBP2 (magenta) and GluA2 (green) to mark synapses, and for Parvalbumin to mark IHCs (blue). Synapse location was determined by using Imaris to derive global image-centric coordinates (yellow axes in A) for each synaptic element and to determine its position within modiolar or pillar regions, as defined for each IHC after transforming to local IHC-centric coordinates (yellow axes in B, see Methods). Images in B are *yz* views of maximum intensity projections along the *x* axis. The projection was clipped to span a single IHC. (**C**) A modest increase in synapse number was observed in *Runx1*^{CKO} mice (15.8±3.0) relative to Control (13.4±3.9) (Wilcoxon Rank Sum Test, p=0.006). (**D**) No change was observed in the proportion of synapses on the modiolar face of IHCs (Control: 0.61±0.19; *Runx1*^{CKO}: 0.65±0.15; t-test, p=0.26). (**E**) Kernel density plots depicting distribution of postsynaptic glutamate receptor (GluA2) patch volumes in Control (left) and *Runx1*^{CKO} (center) groups, separated by modiolar (m, solid line) and pillar (p, dashed line) location; the rightmost plots show the CKO pillar distribution (gray) overlaid with both control distributions. Arrows mark the peak of the distribution for modiolar synapses in CON to highlight rightward shift in the CKO group. (**F**) Two-dimensional density plots of mean GluA2 volumes on modiolar vs. pillar sides of each IHC. Dotted line depicts line of identity corresponding to equal sizes on modiolar and pillar sides. (**G**) Comparison of mean modiolar:pillar GluA2 volume ratio of each IHC. Mean ratio in the Control group was well below 1 (0.62±0.08) and the ratio in the *Runx1*^{CKO} group was significantly higher (0.75±0.06), indicating weakening of the

size gradient (Wilcoxon Rank Sum Test, p=0.036). (**H**) Distribution of presynaptic ribbon volumes in Control and *Runx1*^{CKO} groups, plotted as in E. Arrows indicate peak of modiolar size distribution in CON to highlight leftward shift in the CKO group. Insets show column charts that compare the width of the density curves at 0.5 probability density (gray line) as a measure of spread in size distribution between modiolar (m) and pillar (p) regions. (**I**) Two-dimensional density plots of mean ribbon volumes on modiolar vs. pillar sides of each IHC. Dotted line depicts a line of identity corresponding to equal sizes on modiolar and pillar sides. (**J**) Comparison of mean modiolar:pillar presynaptic ribbon volume ratio of each IHC. Mean ratio in the Control group was above 1 (1.21±0.11), indicating a modiolar-to-pillar gradient. The ratio in the *Runx1*^{CKO} group was significantly lower and below 1 (0.90±0.04), indicating loss of the size gradient (Wilcoxon Rank Sum Test, p=0.028). C,D,G,J are standard box-and-whisker plots with added colored dots denoting groupwise means.

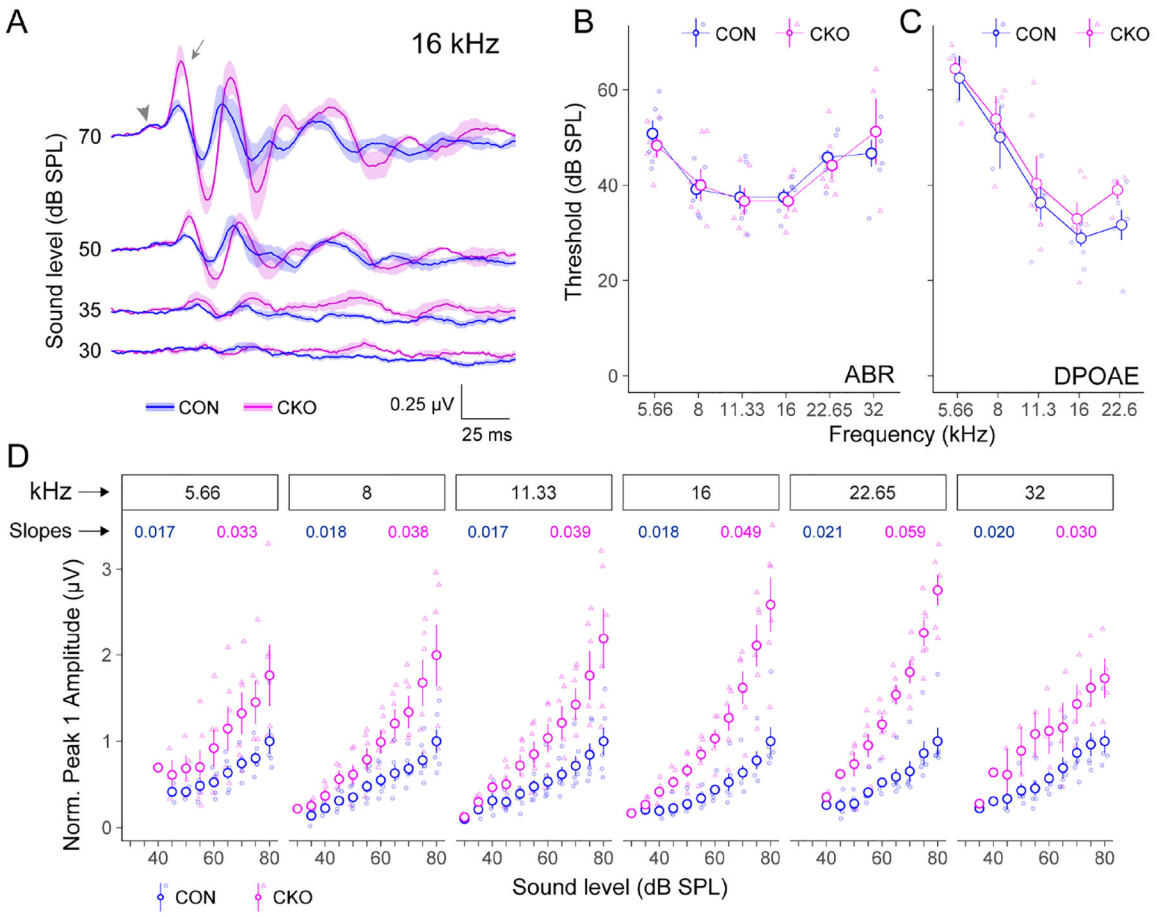

Figure 5: Altered neural response to sound in the cochlea of *Runx1*^{CKO} mice

Auditory brainstem response (ABR) and distortion product otoacoustic emission (DPOAE) were recorded from Control (blue) and *Runx1*^{CKO} (magenta) mice. (**A**) Averaged waveforms of ABRs recorded upon presentation of 16 kHz tone burst at varying sound levels. While SGN responses in peak 1 (arrow) grow as expected with increase in sound level in Control animals, the growth is much larger in the *Runx1*^{CKO} group. Arrowhead indicates summating potential. (**B,C**) No difference in ABR (B) or DPOAE (C) thresholds was observed across all sound frequencies tested (Table S4). Plots share the same y-axis labels. (**D**) Normalized peak 1 amplitude vs. stimulus level plotted for each sound frequency. Plots share the same y-axis. Slopes of the input-output growth functions for the *Runx1*^{CKO} group were larger by a factor of 1.5 or more compared to the Control group. All plots show mean ± SEM for the respective groups. Results of statistical tests for data in B,C,D can be found in Table S4.

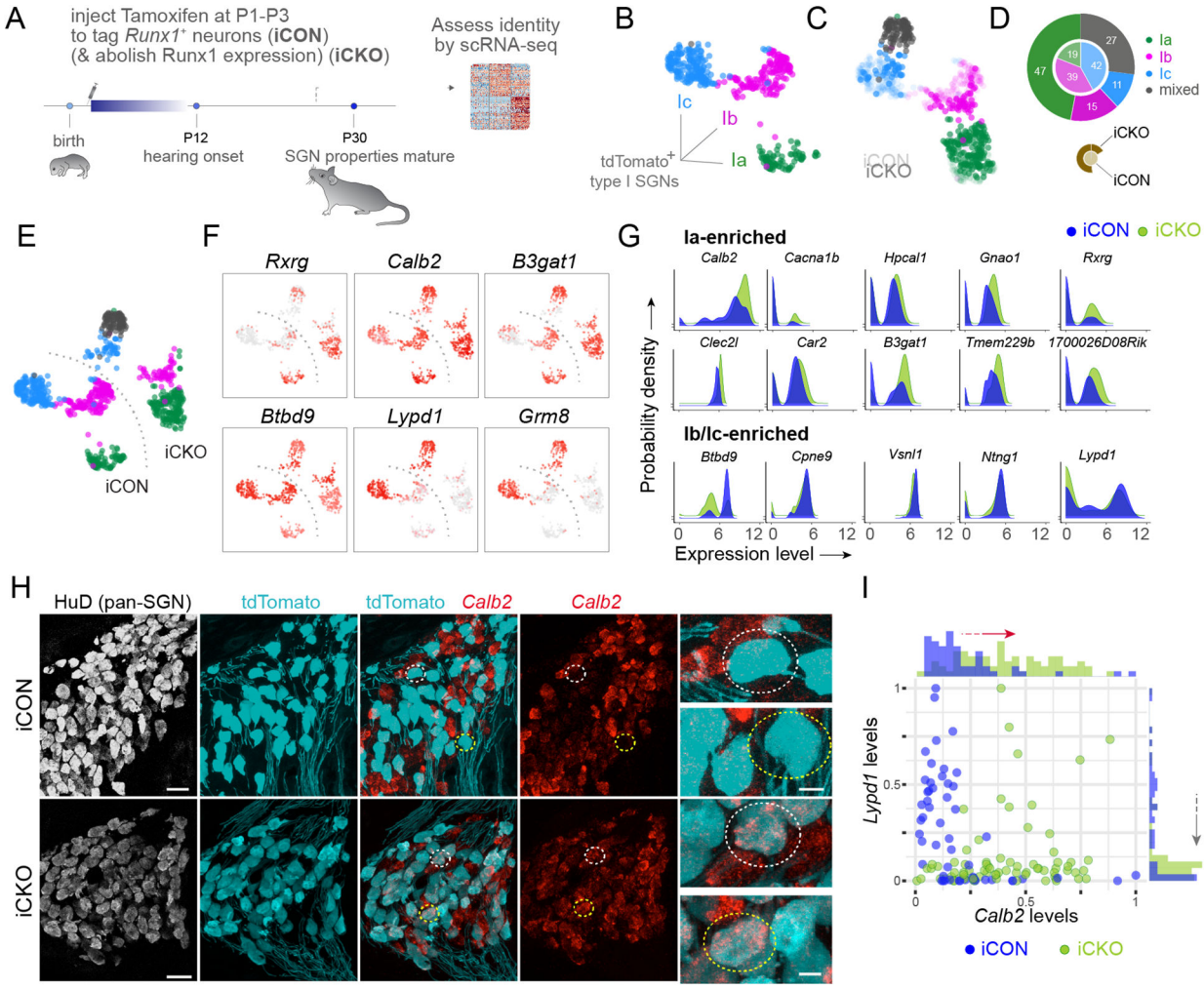

Figure 6: Postnatal *Runx1* loss redirects SGN subtype identities

(**A**) Our scRNA-seq workflow for analyzing Runx1^{+} neurons with (iCKO) or without (iCON) postnatal loss of *Runx1*. (**B**) UMAP embedding of scRNA-seq profiles of iCON SGNs revealed three clusters corresponding to Ia, Ib, Ic subtypes, with most neurons located in the Ib and Ic clusters. (**C**) UMAP embedding of scRNA-seq profiles of SGNs from the iCON (fainter colors) and iCKO (brighter colors) groups revealed that clusters for the two groups largely overlap but differ in terms of cell census. A subset of iCKO cells adjacent to the Ic cluster stands out as a distinct fourth cluster (grey). (**D**) Proportions of SGN subtypes predicted by a supervised classification approach structured to discern Ia, Ib, Ic or mixed identities; numbers indicate % of SGNs in each group. Loss of *Runx1* postnatally resulted in >2.5 fold increase in the proportion of Ia cells at the expense of Ib and Ic identities. In addition, more than a quarter of the SGNs are of mixed identity. (**E**) UMAP embeddings in which SGNs from the two groups and the clusters they fall in are identified, with clusters for each genotype offset as in Figure 1D. (**F**) Feature plots show that the expanded pool of Ia SGNs in iCKO (green) express Ia-(top row) and downregulate Ic-specific (bottom) genes. The fourth cluster (grey in E) contains cells that co-express Ia- and Ic-specific genes. (**G**) Analysis of gene expression patterns without subtype classification

indicates that more SGNs express genes associated with the Ia identity in iCKO (green) compared to iCON (blue) SGNs. (**H, I**) Changes in SGN gene expression patterns were also analyzed by RNAscope on mid-modiolar sections of the P26 cochlea; SGNs visualized by immunostaining for HuD (white) or tdTomato (blue). The *Calb2* gradient (red) was shallower among SGNs of iCKO mice (bottom) than in the iCON group (top). Dotted circles highlight tdTomato+ neurons with low *Calb2* level in the iCON group but high *Calb2* level in the iCKO group. Quantification is shown in a scatterplot of *Calb2* and *Lypd1* levels in fate-mapped tdTomato+ SGNs from iCON (blue) and iCKO (green) animals (I). Histograms depict changed distributions of *Calb2* (top) and *Lypd1* (right) expression levels, respectively. Most iCON SGNs (blue) are $Lypd1^{HI}$ $Calb2^{LOW}$ or $Lypd1^{OFF}$ $Calb2^{LOW}$ (i.e., Ic- or Ib-like, respectively). In contrast, those from iCKO animals (green) are $Lypd1^{OFF}$ $Calb2^{LOW}$ or $Lypd1^{OFF}$ $Calb2^{HI}$ (Ib- or Ia-like, respectively). In addition, a subset of cells is $Lypd1^{HI}$ $Calb2^{HI}$ (i.e., of mixed identity). These trends also hold true at the level of individual genes: histograms show shifts toward higher *Calb2* expression (red arrow, top) and lower *Lypd1* expression (gray arrow, right) among fate-mapped SGNs upon postnatal loss of *Runx1*. Scale bars in H are 20 μm in the HuD panel (left) and 5μm in the insets (right).

Key resources table

REAGENT or RESOURCE	SOURCE	IDENTIFIER
Antibodies		
Mouse anti-CtBP2 IgG1	BD Biosciences	Cat#612044; RRID:AB_399431
Mouse anti-Glutamate Receptor 2, extracellular, clone 6C4 IgG2a	EMD Millipore	Cat#MAB397; RRID:AB_11212990
Rabbit anti-Myosin-VIIa IgG	Proteus Biosciences	Cat#25–6790; RRID:AB_2314838
Chicken anti-Neurofilament H IgY	EMD Millipore	Cat#AB5539; RRID:AB_177520
Rabbit anti-dsRed	Clontech Laboratories	Cat#632496; RRID:AB_10013483
Goat anti-Calretinin	Swant	Cat#CG1; RRID:AB_10000342
Guinea pig anti-Parvalbumin	Synaptic Systems	Cat#195004; RRID:AB_2156476
Mouse anti-HuD (H-9) IgG2a	Santa Cruz Biotechnology	Cat#sc-48421; RRID:AB_627766
Chemicals, peptides, and recombinant proteins		
Tamoxifen	Sigma	Cat# T5648
Corn Oil	Sigma	Cat#C8267
Critical commercial assays		
Chromium Single Cell 3' Next GEM, Library & Gel Bead Kit v3	10x Genomics	Cat#1000075
Chromium Chip B Single Cell Kit	10x Genomics	Cat#1000074
Dual Index Kit Plate TT Set A	10x Genomics	Cat#1000215
NextSeq 500 v2.5 (75 Cycles)	Illumina	Cat#20024906
RNAscope Probe Mm-Calb2-C3	Advanced Cell Diagnostics	Cat#313641-C3
RNAscope Probe Mm-Lypd1	Advanced Cell Diagnostics	Cat#318361
RNAscope Probe Mm-Runx1-C3	Advanced Cell Diagnostics	Cat#406671-C3
RNAscope Multiplex Fluorescent Reagent Kit	Advanced Cell Diagnostics	Cat#320850
Papain	Worthington	Cat#LK003178
Ovomucoid albumin inhibitor	Worthington	Cat#LK003182
DNase	Worthington	Cat#LK003172
Actinomycin D	Sigma-Aldrich	Cat#A1410
Collagenase, Type 4	Worthington	Cat#LS004186
SPRIselect	Beckman Coulter	Cat#B23317
Deposited data		
scRNA-seq data corresponding to results in Figures 2 and 3	This study	GEO: GSE210215
scRNA-seq data corresponding to results in Figures 6	This study	GEO: GSE210216
Data analysis code	This study	GitHub: https://github.com/shrestha-lab/runx1_2023 Zenodo: https://doi.org/10.5281/zenodo.7489992
Experimental models: Organisms/strains		
Mouse: Ai14: *Gt(ROSA)26Sor$^{tm14(CAG-tdTomato)Hze}$*	The Jackson Laboratory	007914; RRID:IMSR_JAX:007914
Mouse: CD1	Charles River Laboratory	022; RRID:IMSR_CRL:22

REAGENT or RESOURCE	SOURCE	IDENTIFIER
Mouse: Runx1$^{f/f:}$*Runx1*$^{tm3.1Spe}$	Nancy A. Speck, PhD Growney et al. (2005)[30]	010673; RRID:IMSR_JAX:010673
Mouse: Ai3: *Gt(ROSA)26Sor*$^{tm3(CAG-EYFP)Hze}$	The Jackson Laboratory	007903; RRID:IMSR_JAX:007903
Mouse: Runx1^{CreER}: Runx1$^{MER-Cre-MER}$	Igor Samokhvalov, PhD RIKEN/ CLST LARGE, Samokhvalov et al. (2007)[28]	N/A
Mouse: *Bhlhe22*^{Cre}*: Bhlhe22*$^{tm3.1(cre)Meg}$	Michael Greenberg; Ross et al., 2010[29]	MGI:4440745
Software and algorithms		
R Project for Statistical Computing, version 4.0.3	CRAN	RRID:SCR_001905
MATLAB v9.10 (R2021a)	Mathworks	RRID:SCR_001622
Fiji	Schindelin et al. (2012)[63]	RRID:SCR_002285
SingleCellNet (R package)	Tan and Cahan (2019)[60]	
DoubletFinder (R package)	McGinnis et al. (2019)[62]	RRID:SCR_018771
Seurat v3 (R package)	Stuart et al. (2019)[58]	RRID:SCR_016341
Imaris v9	Oxford Instruments	RRID:SCR_007370
Integrated Genomics Viewer, v2.15.2	The Broad Institute	RRID:SCR_011793
Other		
10x Chromium Controller	10x Genomics	Cat#120263
MoFlo Astrios EQ Cell Sorter	Beckman Coulter	RRID:SCR_018893